



HAL
open science

A non-intrusive model order reduction approach for parameterized time-domain Maxwell's equations

Kun Li, Ting-Zhu Huang, Liang Li, Ying Zhao, Stéphane Lanteri

► **To cite this version:**

Kun Li, Ting-Zhu Huang, Liang Li, Ying Zhao, Stéphane Lanteri. A non-intrusive model order reduction approach for parameterized time-domain Maxwell's equations. *Discrete and Continuous Dynamical Systems - Series B*, 2022, 28 (1), pp.449-473. 10.3934/dcdsb.2022084 . hal-03922914

HAL Id: hal-03922914

<https://inria.hal.science/hal-03922914>

Submitted on 4 Jan 2023

HAL is a multi-disciplinary open access archive for the deposit and dissemination of scientific research documents, whether they are published or not. The documents may come from teaching and research institutions in France or abroad, or from public or private research centers.

L'archive ouverte pluridisciplinaire **HAL**, est destinée au dépôt et à la diffusion de documents scientifiques de niveau recherche, publiés ou non, émanant des établissements d'enseignement et de recherche français ou étrangers, des laboratoires publics ou privés.

A non-intrusive model order reduction approach for parameterized time-domain Maxwell's equations

Kun Li^a, Ting-Zhu Huang^{b,*}, Liang Li^{b,*}, Ying Zhao^b, Stéphane Lanteri^c

^a*School of Mathematics, Southwestern University of Finance and Economics, Chengdu, P.R. China*

^b*School of Mathematical Sciences, University of Electronic Science and Technology of China, Chengdu, P.R. China*

^c*Université Côte d'Azur, Inria, CNRS, LJAD, Sophia Antipolis Cedex, France*

Abstract

We present a non-intrusive model order reduction (NIMOR) method with an offline-online decoupling for the solution of parameterized time-domain Maxwell's equations. During the offline stage, the training parameters are chosen by using Smolyak sparse grid method with an approximation level L ($L \geq 1$) over a target parameterized space. This method can deal with the so-called *curse of dimensionality* in high dimensional space. For each selected parameter, the snapshot vectors are first produced by a high order discontinuous Galerkin time-domain (DGTD) solver formulated on an unstructured simplicial mesh. In order to minimize the overall computational cost in the offline stage and to improve the accuracy of the NIMOR method, a radial basis function (RBF) interpolation method is then used to construct more snapshot vectors at the sparse grid with approximation level $L + 1$, which includes the sparse grids from approximation level L . A nested proper orthogonal decomposition (POD) method is employed to extract time- and parameter-independent POD basis functions. By using the singular value decomposition (SVD) method, the principal components of the reduced coefficient matrices of the high-fidelity solutions onto the reduced-order subspace spanned by the POD basis functions are extracted. Moreover, a Gaussian process regression (GPR) method is proposed to approximate the dominating time- and parameter-modes of the reduced coefficient matrices. During the online stage, the reduced-order solutions for new time and parameter values can be rapidly recovered via outputs from the regression models without using the DGTD method. The performance of this NIMOR method is illustrated numerically by considering two classical test cases: the scattering of a plane wave by a 2-D dielectric disk and the scattering of a plane wave by a multi-layer heterogeneous medium. The prediction capabilities of the NIMOR method are evaluated by varying the relative permittivity. Numerical results indicate that the NIMOR method is a promising approach for simulating accurately and in fast way parameterized time-domain electromagnetic problems.

Keywords: non-intrusive model order reduction; Smolyak sparse grid; proper orthogonal decomposition; gaussian process regression; parameterized time-domain Maxwell's equations.

*Corresponding author

Email addresses: rclikun@163.com, likun@swufe.edu.cn (Kun Li), tzhuang@uestc.edu.cn (Ting-Zhu Huang), plum_liliang@uestc.edu.cn, plum.liliang@gmail.com (Liang Li), yinger_z@126.com (Ying Zhao), Stephane.Lanteri@inria.fr (Stéphane Lanteri)

1. Introduction

In computational electromagnetics, the discontinuous Galerkin time-domain (DGTD) method, which can be regarded as a combination of the finite element (FE) and finite volume (FV) methods [1], has become a popular high fidelity method during the last ten years because of its salient features, e.g., high order accuracy, local approximation order strategy [2], isoparametric curvilinear meshes [3], and natural parallelism [4]. However, it suffers from a drawback that the number of degrees of freedom (DoFs) is usually much larger than that of a conforming FE method. This problem becomes more troublesome when one needs to repeatedly solve the high dimensional model (HDM) over a large number of parameter values, like in multi-query analysis including design, control, optimization, and uncertainty quantification (UQ) [5, 6, 7]. In this context, when the incident directions, boundary conditions, geometric features, or the material properties vary a little, we are expecting that the solutions are closely related. Based on this idea, one could construct a reduced-order model (ROM) by using efficient model order reduction (MOR) methods dramatically reducing the number of DoFs. The overall goal of the MOR method is to reduce the computational cost by several orders of magnitude while maintaining an acceptable level of accuracy [8, 9].

The *reduced basis* (RB) method with an *offline-online* framework is a well-known and widely used MOR method [10, 11, 12]. The starting point of the MOR method during the offline stage is a sampling of high fidelity snapshots at some time/parameter locations from numerical simulations or experiments. The simplest sampling method is the uniform sampling manner [11, 12], which leads to the so-called *curse of dimensionality* in high dimensional parameter space. Another similar approach is the random sampling method, e.g., latin hyper-cube sampling (LHS) [13]. In order to deal with this problem, the Smolyak sparse grid technique is used to generate the parameter points in high dimensional space [14, 15]. Its key idea is that it selects a relatively small number of nodes on the full tensor-product grid of parameter values in terms of potential importance of the nodes, thus resulting in improved computational efficiency. The above three sampling strategies are the priori methods [16], and the selection of sampling points only depends on the information contained in the parameter space itself. Another type of sampling approach is the posterior method, in which the sampling of snapshots relies on the error information of the ROM [10, 17, 18]. However, it should be noted that the posterior method is not feasible for problems without a natural criterion for the selection of snapshots.

In a second step, a set of RB functions are extracted from the collection of high fidelity snapshots. The proper orthogonal decomposition (POD) method, also known as Karhunen-Loeve expansion, principal component analysis, or singular value decomposition, is a popular RB function generation approach [7, 19, 20, 21]. This method is applicable to a wide range of problems, including time-dependent and nonlinear problems. The reduced space is spanned by the RB functions (also termed as POD basis functions), which captures the dominant features of the original full-order system. Then the reduced-order approximations are expressed as linear combinations of these basis functions.

To determine the reduced-order coefficients or the expansion coefficients of the POD basis functions during the online stage, MOR methods are generally grouped into two families: *intrusive* MOR (IMOR) and *non-intrusive* MOR (NIMOR) methods. In IMOR method, the POD method combined with projection techniques are usually used to reduce the complexity of classical numerical methods, such as the finite difference (FD) [22, 23, 24], FE [25, 26, 27], FV [28, 29, 30], hybridizable discontinuous Galerkin (HDG) [8], and DGTD [31, 32] methods, where the Galerkin procedure is the most popular choice for the projection [11]. Besides, in order to avoid the unrewarding repeated computations in the IMOR methods, some reduced-order extrapolated schemes have successively been established by Luo's research team since 2013 [33, 34, 35, 36, 37, 38, 39, 40]. The IMOR method is very straightforward to apply to linear

PDEs, but it poses severe challenges to PDEs that have nonlinear terms and complex parameter dependencies (such as geometric shape or size parameters). For these problems, it is necessary to take additional steps commonly referred to as *hyper-reduction* to effectively approximate the nonlinear term or the projection of the non-affine transformation, such as the empirical interpolation method (EIM) [41] and its corresponding discrete method (DEIM) [42]. Moreover, the IMOR method requires access to the original HDM, leading to some expertise requirements for users in terms of numerical calculations and analysis capabilities [14].

Different from the IMOR method, the NIMOR method only uses the approximation mappings obtained by some data-driven methods [43], such as interpolation, regression, and artificial neural networks (ANN) methods, to calculate the reduced-order coefficients for new time/parameter values. There has been a lot of work [9, 10, 11, 17, 14, 18, 44, 45, 46, 47, 48, 49] on the NIMOR method in the very recent years. Audouze *et al.* in [44] present a NIMOR method for nonlinear parametric time dependent PDEs using POD and radial basis function (RBF) approximation. In [10], Gaussian process regression (GPR) is utilized as the regression model for nonlinear structural analysis, and three numerical examples are employed to demonstrate the effectiveness of the proposed NIMOR method. Hesthaven and Ubbiali in [12] employ an ANN to compute the reduced-order coefficients of the ROM, where the nonlinear Poisson and steady-state incompressible Navier-Stokes equations are tested. In [48], the polynomial chaos expansion (PCE) method is used in the NIMOR method for stochastic representations in UQ analysis. The GPR method is a machine learning regression method based on Bayesian and statistical theories, which is suitable for dealing with complex problems such as high dimensions, small samples and nonlinearity. Compared with the ANN, it comes with advantages such as easy implementation, adaptive acquisition of hyperparameters, and probabilistic output.

However, the drawback of the NIMOR method is the high cost of the offline stage, since a large number of high-fidelity simulations are needed to generate a sufficiently large data set to train an accurate regression model [50]. Therefore, we consider a NIMOR method based on the Smolyak sparse grid, RBF and GPR methods for parameterized time-domain Maxwell's equations in this study, which is different from our previous work [9], in which the training parameter samples are generated via uniform sampling and the cubic spline interpolation-based approach is proposed to approximate the dominating time- and parameter-modes of the reduced coefficient matrices. [In current work, a small size snapshot set is firstly generated from a high fidelity DGTD solver at the Smolyak sparse grid with approximation level \$L\$ \(\$L \geq 1\$ \), and the RBF method is then used to produce more snapshot vectors at the sparse grid with approximation level \$L + 1\$ to minimize the overall computational offline cost and improve the accuracy of the NIMOR method.](#) A nested POD method is applied for the parameterized time-domain problem, where the POD method is implemented separately for time and parameter spaces. Moreover, the GPR method is proposed to approximate the dominating time- and parameter-modes of the reduced coefficient matrices. The main outcome of our study lies in the numerical demonstration of the effectiveness of the proposed NIMOR method for the simulation of parametrized time-domain electromagnetic wave propagation in homogeneous media and heterogeneous media as well.

The remainder of this paper is organized as follows. We briefly introduce the DGTD formulation of the time-domain Maxwell's equations in Section 2. Section 3 describes the computation of the POD basis function. Section 4 presents the NIMOR method. Section 5 presents and discusses some numerical results for the scattering of a plane wave by a 2-D dielectric disk and a multi-layer heterogeneous medium. Section 6 concludes this study.

2. Mathematical modeling

We consider the fullwave model governed by the parameterized time-domain Maxwell's equations augmented with the Silver-Müller absorbing boundary condition (ABC) and the initial conditions

$$\begin{cases} \mu_r \frac{\partial \mathbf{H}(\mathbf{x}, t)}{\partial t} + \text{curl}(\mathbf{E}(\mathbf{x}, t)) = 0, & \forall (\mathbf{x}, t) \in \Omega \times \mathcal{T}, \\ \varepsilon_r \frac{\partial \mathbf{E}(\mathbf{x}, t)}{\partial t} - \text{curl}(\mathbf{H}(\mathbf{x}, t)) = 0, & \forall (\mathbf{x}, t) \in \Omega \times \mathcal{T}, \\ \mathcal{L}(\mathbf{E}(\mathbf{x}, t), \mathbf{H}(\mathbf{x}, t)) = \mathcal{L}(\mathbf{E}^{inc}(\mathbf{x}, t), \mathbf{H}^{inc}(\mathbf{x}, t)), & \forall (\mathbf{x}, t) \in \partial\Omega \times \mathcal{T}, \\ \mathbf{E}(\mathbf{x}, 0) = \mathbf{E}_0(\mathbf{x}), \quad \mathbf{H}(\mathbf{x}, 0) = \mathbf{H}_0(\mathbf{x}), & \forall \mathbf{x} \in \Omega, \end{cases} \quad (1)$$

where $\mathcal{T} = [0, T_f]$ is the target time window, Ω is the spatial domain with a boundary $\partial\Omega$, \mathbf{E} and \mathbf{H} respectively denote the electric and magnetic fields; ε_r and μ_r represent the relative permittivity and permeability, \mathcal{L} is defined as $\mathcal{L}(\mathbf{E}(\mathbf{x}, t), \mathbf{H}(\mathbf{x}, t)) = \mathbf{n} \times \mathbf{E}(\mathbf{x}, t) + Z\mathbf{n} \times (\mathbf{n} \times \mathbf{H}(\mathbf{x}, t))$, with $Z = \sqrt{\mu_r/\varepsilon_r}$, \mathbf{E}^{inc} and \mathbf{H}^{inc} describing the incident fields, and \mathbf{n} standing for the outer unit normal vector on $\partial\Omega$; \mathbf{E}_0 and \mathbf{H}_0 are some predefined functions. In this study, we only consider $\theta = (\varepsilon_{r,1}, \varepsilon_{r,2}, \dots, \varepsilon_{r,p}) \in \mathcal{P} \subset \mathcal{R}^p$ as the problem's parameters with $\varepsilon_{r,i}$ ($i = 1, 2, \dots, p$) being the relative permittivity in the i -th domain of Ω , \mathcal{P} being the parameter domain, and p being the number of parameters.

To obtain high fidelity solutions of system (1), we resort to a high order in space discontinuous Galerkin (DG) method with the second order leap-frog (LF₂) time stepping schem. The resulting method is referred as the discontinuous Galerkin time-domain (DGTD) method. Based on the time partition $0 = t^{(0)} < t^{(1)} < \dots < t^{(\mathcal{N}_t)} = T_f$ with $t^{(n)} = n\Delta t$ ($n = 0, 1, \dots, \mathcal{N}_t$) and Δt denoting the time step size, the DGTD fully discrete scheme is defined as

$$\begin{cases} \mathbb{M}^{\varepsilon_r} \frac{\underline{\mathbf{E}}_h^{(n+1)} - \underline{\mathbf{E}}_h^{(n)}}{\Delta t} = (\mathbb{K} - \mathbb{S}^i) \underline{\mathbf{H}}_h^{(n+\frac{1}{2})} - \mathbb{S}^h \widehat{\underline{\mathbf{H}}}_h^{(n+\frac{1}{2})} - \mathbf{B}^h(n\Delta t), \\ \mathbb{M}^{\mu_r} \frac{\underline{\mathbf{H}}_h^{(n+\frac{3}{2})} - \underline{\mathbf{H}}_h^{(n+\frac{1}{2})}}{\Delta t} = (-\mathbb{K} + \mathbb{S}^i) \underline{\mathbf{E}}_h^{(n+1)} + \mathbb{S}^e \widehat{\underline{\mathbf{E}}}_h^{(n+1)} + \mathbf{B}^e((n + \frac{1}{2})\Delta t), \end{cases} \quad (2)$$

in which $\underline{\mathbf{E}}_h$ and $\underline{\mathbf{H}}_h$ are $\mathcal{N}_d \times 1$ vector solutions with \mathcal{N}_d being the corresponding spatial DoFs; $\mathbb{M}^{\varepsilon_r}$ and \mathbb{M}^{μ_r} are the symmetric positive definite mass matrices, \mathbb{K} is the symmetric stiffness matrix, \mathbb{S}^i is the symmetric surface matrix for the interior faces, and \mathbb{S}^h and \mathbb{S}^e are the skew-symmetric boundary face matrices; \mathbf{B}^e and \mathbf{B}^h are the $\mathcal{N}_d \times 1$ vectors account for the boundary condition. Detailed derivation and definition of these matrices can be found in [32].

3. Computation of the POD basis functions

3.1. Choice of the parameter points using Smolyak sparse grid

The Smolyak sparse grid is often used for the integration or interpolation of multivariate functions, which can deal with the so-called *curse of dimensionality* problem in high dimensional space. **The core idea of the Smolyak sparse grid is that it selects relatively few nodes on the full tensor product grid according to the potential importance of the nodes, thereby improving computational efficiency under the interpolation error as close as possible to the full grid method.** For a more detailed introduction of this technique, see [51, 52]. In the following, the process of sampling the parameter interpolation points over the parameter space \mathcal{P} will be briefly introduced.

Let Q_{i_k} be an interpolation operator in the k th-direction. The interpolation operator of Smolyak algorithm in whole p -dimensional space can be expressed as

$$Q(L, p) = \sum_{L-p+1 \leq |i| \leq L} (-1)^{L-|i|} \binom{p-1}{L-|i|} (Q_{i_1} \otimes Q_{i_2} \otimes \cdots \otimes Q_{i_p}), \quad (3)$$

where \otimes is the tensor product operator, i_k ($k = 1, 2, \dots, p$) denotes the approximation level of the sparse grid in the k th-direction, L is the entire approximation level of the sparse grid, and $|i| = i_1 + i_2 + \cdots + i_p$. According to (3), we only need to know the function values of the desired function on the sparse grid, but not the function values on the full grid. The set of sparse sampling points in (3) can then be expressed as

$$\Theta(L, p) = \bigcup_{L-p+1 \leq |i| \leq L} (\Theta_1^{i_1} \otimes \Theta_1^{i_2} \otimes \cdots \otimes \Theta_p^{i_p}), \quad (4)$$

with

$$\Theta_k^l = \{\alpha_k^{(1)}, \alpha_k^{(2)}, \dots, \alpha_k^{(M_k^l)}\},$$

where Θ_k^l is the vector of sampling points with the approximation level l in the k th-direction, and M_k^l denotes the corresponding number of sampling points. As the approximation level is increased, a larger number of nodes will be used and higher approximation quality will be obtained. If the sampling points in each dimension are nested, i.e., $\Theta_k^l \subset \Theta_k^j$, $l < j$, $k = 1, 2, \dots, p$, then the total number of sampling points in the Smolyak sparse grid can be minimized. In particular, the finally constructed high dimensional sparse points also inherit this nesting feature. For example, one can choose the following Clenshaw-Curtis points [53] as the sampling points on each dimension

$$\alpha_k^{(j)} = \begin{cases} 0, & \text{if } l = 0, \\ -\cos \frac{(j-1)\pi}{M_k^l - 1}, & j = 1, 2, \dots, M_k^l, \text{ if } l > 0, \end{cases} \quad (5)$$

and

$$M_k^l = \begin{cases} 1, & \text{if } l = 0, \\ 2^l + 1, & \text{if } l > 0. \end{cases} \quad (6)$$

In one-dimensional cases, the Smolyak sparse grids with the approximation levels 0, 1, 2, 3 are shown in Figure 1. It is evident that the set of sparse sampling points are nested, i.e., $\Theta_1^l \subset \Theta_1^{l+1}$. In two-dimensional cases, the Smolyak sparse grid with the approximation level 3 and the corresponding full tensor grid are illustrated in Figure 2. One can find that the full tensor product grid has $9 \times 9 = 81$ points, while the Smolyak sparse grid only has 29 points. A comparison of the number of sampling points using Smolyak sparse grid and full tensor product grid with the approximation levels 2, 3, and 5 in 2, 5, and 10-dimensional parameter space is shown in Table 1, respectively. With the increase of dimension size p , although the number of sampling points in the Smolyak sparse grids also increases notably, the curse of dimensionality is significantly suppressed compared with the full tensor product grids. In our case, the Smolyak sparse grid will be used to select the training parameter sets.

3.2. Interpolation of snapshots using RBF method

Let $\mathcal{P}_{tr}(L, p) = \Theta(L, p) = \{\theta^{(1)}; \theta^{(2)}; \dots; \theta^{(\mathcal{N}_p^L)}\} \subset \mathcal{P}$ be the training parameter set chosen by the Smolyak sparse grid technique, where \mathcal{N}_p^L is the number of sampling points with the entire approximation level L in the p -dimension parameter space, and $\theta^{(i)} \in \mathcal{R}^p$ ($i = 1, 2, \dots, \mathcal{N}_p^L$).

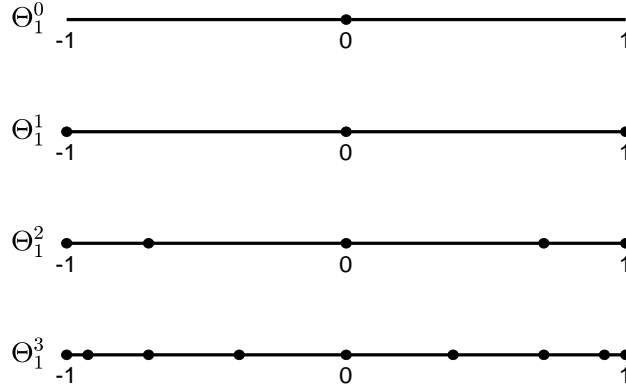


Figure 1: 1-D Smolyak sparse grids with approximation level 0, 1, 2, 3.

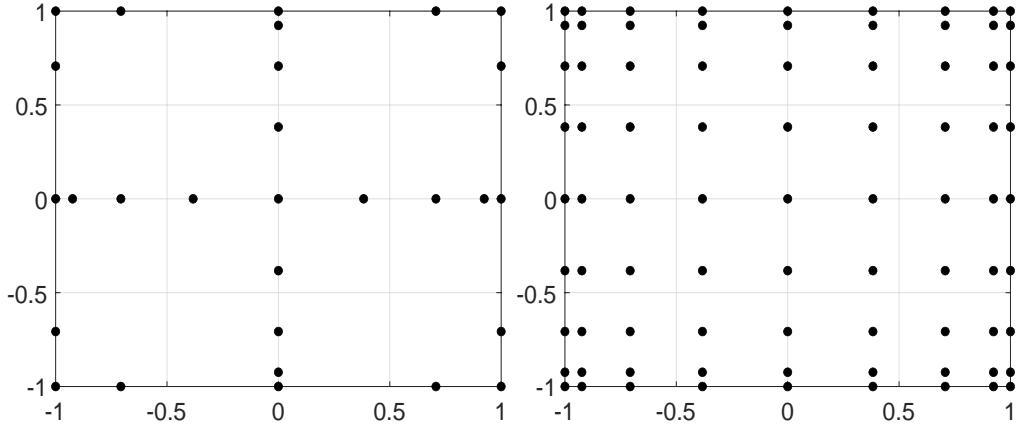


Figure 2: 2-D Smolyak sparse grid with approximation level 3 and full tensor product grid.

Table 1: Comparison of the number of sampling points using Smolyak sparse grid and full tensor product grid. Here M_1 is the number of sampling points using Smolyak sparse grid, and M_2 is the number of sampling points using full tensor product grid.

Dimension size p	Approximation level l	M_1	M_2	$\frac{M_2}{M_1}$
2	2	13	25	1.923
	3	29	81	2.793
	5	145	1089	7.510
5	2	61	3125	51.230
	3	241	59049	2.450×10^2
10	5	2433	3.914×10^7	1.609×10^4
	2	221	9.766×10^6	4.419×10^4
	3	1581	3.487×10^9	2.206×10^6
	5	41265	1.532×10^{15}	3.713×10^{10}

For the training parameters $\theta^{(i)} \in \mathcal{P}_{tr}(L, p)$, the corresponding high fidelity solutions can be obtained by using the DGTD method. The time trajectory matrix, for example, $\mathbb{A}_{\mathbf{E}}^i$, at the time steps $t^{(n_i)} \in \mathcal{T}_{tr} = \{t^{(n_1)}, t^{(n_2)}, \dots, t^{(n_{\mathcal{N}_t})}\} \subset \mathcal{T}$ is expressed as

$$\mathbb{A}_{\mathbf{E}}^i = \begin{pmatrix} \underline{\mathbf{E}}_{h,1}^{(n_1)}(\theta^{(i)}) & \underline{\mathbf{E}}_{h,1}^{(n_2)}(\theta^{(i)}) & \dots & \underline{\mathbf{E}}_{h,1}^{(n_{\mathcal{N}_t})}(\theta^{(i)}) \\ \underline{\mathbf{E}}_{h,2}^{(n_1)}(\theta^{(i)}) & \underline{\mathbf{E}}_{h,2}^{(n_2)}(\theta^{(i)}) & \dots & \underline{\mathbf{E}}_{h,2}^{(n_{\mathcal{N}_t})}(\theta^{(i)}) \\ \vdots & \vdots & \ddots & \vdots \\ \underline{\mathbf{E}}_{h,\mathcal{N}_d}^{(n_1)}(\theta^{(i)}) & \underline{\mathbf{E}}_{h,\mathcal{N}_d}^{(n_2)}(\theta^{(i)}) & \dots & \underline{\mathbf{E}}_{h,\mathcal{N}_d}^{(n_{\mathcal{N}_t})}(\theta^{(i)}) \end{pmatrix} \in \mathcal{R}^{\mathcal{N}_d \times \mathcal{N}_t}, \quad i = 1, 2, \dots, \mathcal{N}_p^L, \quad (7)$$

and then the snapshot matrix for all parameters in $\mathcal{P}_{tr}(L, p)$ is

$$\mathbb{A}_{\mathbf{E}} = \begin{bmatrix} \mathbb{A}_{\mathbf{E}}^1 & \mathbb{A}_{\mathbf{E}}^2 & \dots & \mathbb{A}_{\mathbf{E}}^{\mathcal{N}_p^L} \end{bmatrix} \in \mathcal{R}^{\mathcal{N}_d \times \mathcal{N}_{tp}^L}, \quad (8)$$

where \mathcal{N}_d is the number of DoF of the DGTD method, and $\mathcal{N}_{tp}^L = \mathcal{N}_t \times \mathcal{N}_p^L$ is the number of all snapshots. Similarly, one can obtain the snapshot matrix $\mathbb{A}_{\mathbf{H}} \in \mathcal{R}^{\mathcal{N}_d \times \mathcal{N}_{tp}^L}$ for the magnetic field of the training parameter set $\mathcal{P}_{tr}(L, p)$. In particular, one should obtain as many snapshots as possible to improve the accuracy of the NIMOR method over the target parameterized space \mathcal{P} , which is time-consuming, especially for many 2-D and 3-D problems. In order to minimize the overall computational offline cost and improve the accuracy of the NIMOR method, a radial basis function (RBF) interpolation method is used to construct the snapshot vectors at higher approximation level of the Smolyak sparse grid.

Let $\mathcal{F}_{\mathbf{u}}(\theta)$ denotes the interpolation function representing $\underline{\mathbf{u}}_h(\cdot, \cdot, \theta)$ ($\mathbf{u} \in \{\mathbf{E}, \mathbf{H}\}$), and having the following form

$$\mathcal{F}_{\mathbf{u}}(\theta) = \sum_{i=1}^{\mathcal{N}_p^L} \omega_{\mathbf{u},i} \varphi(\|\theta - \theta^{(i)}\|), \quad (9)$$

where $\omega_{\mathbf{u},i}$ is the weight associated with the parameter $\theta^{(i)}$, $\|\cdot\|$ denotes the norm of a vector, usually chosen as Euclidean distance, and $\varphi(\cdot)$ is the RBF. The frequently used RBFs can be either multi-quadric, inverse quadratic, Gaussian, plate spline or inverse multi-quadric. In this study, we choose the Gaussian RBF, which has a form of $\varphi(r) = e^{-\left(\frac{r}{\sigma}\right)^2}$ with r being the radius and σ being the shape parameter. The weights $\omega_{\mathbf{u}}(k, j) = [\omega_{\mathbf{u},1}(k, j), \omega_{\mathbf{u},2}(k, j), \dots, \omega_{\mathbf{u},\mathcal{N}_p^L}(k, j)]^T$ at k th space point and n_j th time point can be obtained by solving the following linear equation

$$\mathcal{A} \omega_{\mathbf{u}}(k, j) = \mathcal{B}_{\mathbf{u}}(k, j), \quad (10)$$

where $\mathcal{B}_{\mathbf{u}}(k, j) = [\underline{\mathbf{u}}_{h,k}^{(n_j)}(\theta^{(1)}), \underline{\mathbf{u}}_{h,k}^{(n_j)}(\theta^{(2)}), \dots, \underline{\mathbf{u}}_{h,k}^{(n_j)}(\theta^{(\mathcal{N}_p^L)})]^T$, and

$$\mathcal{A} = \begin{pmatrix} \varphi(\|\theta^{(1)} - \theta^{(1)}\|) & \varphi(\|\theta^{(1)} - \theta^{(2)}\|) & \dots & \varphi(\|\theta^{(1)} - \theta^{(\mathcal{N}_p^L)}\|) \\ \varphi(\|\theta^{(2)} - \theta^{(1)}\|) & \varphi(\|\theta^{(2)} - \theta^{(2)}\|) & \dots & \varphi(\|\theta^{(2)} - \theta^{(\mathcal{N}_p^L)}\|) \\ \vdots & \vdots & \ddots & \vdots \\ \varphi(\|\theta^{(\mathcal{N}_p^L)} - \theta^{(1)}\|) & \varphi(\|\theta^{(\mathcal{N}_p^L)} - \theta^{(2)}\|) & \dots & \varphi(\|\theta^{(\mathcal{N}_p^L)} - \theta^{(\mathcal{N}_p^L)}\|) \end{pmatrix}.$$

For a new arbitrary parameter point $\theta^{\text{new}} \in \mathcal{R}^p$ within the parameter set $\mathcal{P}_{tr}(L+1, p)$ ($L \geq 1$) with the entire approximation level $L+1$ in the p -dimension parameter space, the snapshot vector $\underline{\mathbf{E}}_{h,k}^{(n_j)}(\theta^{\text{new}})$ at k th space point and n_j th time point can be calculated as

$$\underline{\mathbf{E}}_{h,k}^{(n_j)}(\theta^{\text{new}}) = \sum_{i=1}^{\mathcal{N}_p^L} \omega_{\mathbf{u},i}(k, j) \varphi(\|\theta^{\text{new}} - \theta^{(i)}\|), \quad k = 1, 2, \dots, \mathcal{N}_d, \quad j = 1, 2, \dots, \mathcal{N}_t. \quad (11)$$

The construction of the snapshots over the training parameter set $\mathcal{P}_{tr}(L+1, p)$ ($L \geq 1$) is summarized in Algorithm 1.

Algorithm 1 Construction of the snapshots over the training parameter set $\mathcal{P}_{tr}(L+1, p)$ ($L \geq 1$)

Input: Training parameter sets $\mathcal{P}_{tr}(L, p)$ and $\mathcal{P}_{tr}(L+1, p)$ ($L \geq 1$), and shape parameter σ

Output: Snapshot matrix $\mathbb{A}_{\mathbf{u}}$ ($\mathbf{u} \in \{\mathbf{E}, \mathbf{H}\}$) in $\mathcal{P}_{tr}(L+1, p)$

- 1: Compute the high fidelity solutions $\underline{\mathbf{u}}_{h,k}^{(n_j)}(\theta^i)$ via the DGTD method in the domain $\Omega \times \mathcal{T}$, $\theta^i \in \mathcal{P}_{tr}(L, p)$, $\mathbf{u} \in \{\mathbf{E}, \mathbf{H}\}$;
 - 2: Compute the weights $\omega_{\mathbf{u}}(k, j)$ for the k th space point and the n_j th time point via (10);
 - 3: Obtain the snapshot $\underline{\mathbf{u}}_{h,k}^{(n_j)}(\theta^q)$ for new arbitrary parameter point $\theta^q \in \mathcal{P}_{tr}(L+1, p) \setminus \mathcal{P}_{tr}(L, p)$ via (11);
 - 4: Construct the snapshot matrix $\mathbb{A}_{\mathbf{u}}$ similar to (7) and (8).
-

3.3. Nested proper orthogonal decomposition

The singular value decomposition (SVD) of the snapshot matrix $\mathbb{A}_{\mathbf{u}}$ is performed as

$$\mathbb{A}_{\mathbf{u}} = \mathbb{U}_{\mathbf{u}} \Sigma_{\mathbf{u}} \mathbb{V}_{\mathbf{u}}^T = \sum_{i=1}^{r_{\mathbf{u}}} \sigma_{\mathbf{u},i} \phi_{\mathbf{u},i} \psi_{\mathbf{u},i}^T, \quad \mathbf{u} \in \{\mathbf{E}, \mathbf{H}\}, \quad (12)$$

where $\Sigma_{\mathbf{u}} = \text{diag}(\sigma_{\mathbf{u},1}, \sigma_{\mathbf{u},2}, \dots, \sigma_{\mathbf{u},r_{\mathbf{u}}}, 0, \dots, 0)$ with $\sigma_{\mathbf{u},1} \geq \sigma_{\mathbf{u},2} \geq \dots \geq \sigma_{\mathbf{u},r_{\mathbf{u}}} > 0$ being the singular values of $\mathbb{A}_{\mathbf{u}}$ and $r_{\mathbf{u}} \leq \min\{\mathcal{N}_d, \mathcal{N}_{tp}^{L+1}\}$ being the rank of $\mathbb{A}_{\mathbf{u}}$, and $\mathbb{U}_{\mathbf{u}} = [\phi_{\mathbf{u},1}, \phi_{\mathbf{u},2}, \dots, \phi_{\mathbf{u},\mathcal{N}_d}]$ and $\mathbb{V}_{\mathbf{u}} = [\psi_{\mathbf{u},1}, \psi_{\mathbf{u},2}, \dots, \psi_{\mathbf{u},\mathcal{N}_{tp}^{L+1}}]$ are orthogonal matrices with $\phi_{\mathbf{u},i}$ and $\psi_{\mathbf{u},i}$ being the left and right singular vectors of $\mathbb{A}_{\mathbf{u}}$. For numerical stability and/or to reduce the computation cost, one may also first construct the correlation matrix $\mathbb{C}_{\mathbf{u}} = \mathbb{A}_{\mathbf{u}}^T \mathbb{A}_{\mathbf{u}}$ of snapshot matrix $\mathbb{A}_{\mathbf{u}}$ and compute the corresponding eigenvalue decomposition, especially when the number of snapshots \mathcal{N}_{tp}^{L+1} is much smaller than the number of DoF \mathcal{N}_d . Given any $k_{\mathbf{u}}$ ($k_{\mathbf{u}} \ll r_{\mathbf{u}}$), the POD basis function is defined to be the set $\{\phi_{\mathbf{u},i}\}_{i=1}^{k_{\mathbf{u}}}$ in model order reduction, which can be used to construct the reduced basis subspace $\mathcal{V}_{rb,\mathbf{u}} = \text{span}\{\phi_{\mathbf{u},1}, \phi_{\mathbf{u},2}, \dots, \phi_{\mathbf{u},k_{\mathbf{u}}}\}$. According to Schmidt-Eckart-Young (S-E-Y) theorem, the POD basis functions of rank $k_{\mathbf{u}}$ minimize the projection error, i.e.,

$$\begin{aligned} \sum_{j=1}^{\mathcal{N}_p^{L+1}} \sum_{i=1}^{\mathcal{N}_t} \|\mathbb{A}_{\mathbf{u}}^j(:, i) - \mathbb{P}_{\mathbf{u}} \mathbb{P}_{\mathbf{u}}^T \mathbb{A}_{\mathbf{u}}^j(:, i)\|_{\mathcal{R}^{\mathcal{N}_d}}^2 &= \min_{\mathbb{W}_{\mathbf{u}} \in \Pi_{k_{\mathbf{u}}}} \sum_{j=1}^{\mathcal{N}_p^{L+1}} \sum_{i=1}^{\mathcal{N}_t} \|\mathbb{A}_{\mathbf{u}}^j(:, i) - \mathbb{W}_{\mathbf{u}} \mathbb{W}_{\mathbf{u}}^T \mathbb{A}_{\mathbf{u}}^j(:, i)\|_{\mathcal{R}^{\mathcal{N}_d}}^2 \\ &= \sum_{i=k_{\mathbf{u}}+1}^{r_{\mathbf{u}}} \sigma_{\mathbf{u},i}^2, \quad \mathbf{u} \in \{\mathbf{E}, \mathbf{H}\}, \end{aligned} \quad (13)$$

where $\mathbb{P}_{\mathbf{u}} = [\phi_{\mathbf{u},1}, \phi_{\mathbf{u},2}, \dots, \phi_{\mathbf{u},k_{\mathbf{u}}}]$ is the basis matrix comprising the first $k_{\mathbf{u}}$ left singular vectors of $\mathbb{A}_{\mathbf{u}}$, $\mathbb{A}_{\mathbf{u}}^j(:, i)$ is the i -th column of $\mathbb{A}_{\mathbf{u}}^j$ ($j = 1, 2, \dots, \mathcal{N}_p^{L+1}$), and $\Pi_{k_{\mathbf{u}}} = \{\mathbb{W}_{\mathbf{u}} \in \mathcal{R}^{\mathcal{N}_d \times k_{\mathbf{u}}} : \mathbb{W}_{\mathbf{u}}^T \mathbb{W}_{\mathbf{u}} = \mathbb{I}_{k_{\mathbf{u}}}\}$ is the set of all $k_{\mathbf{u}}$ -dimensional orthogonal basis functions. The dimension $k_{\mathbf{u}}$ of the POD basis is then determined by the criterion

$$k_{\mathbf{u}} = \text{argmin}\{\mathcal{E}(k_{\mathbf{u}}) : \mathcal{E}(k_{\mathbf{u}}) \geq 1 - \rho\}, \quad \mathbf{u} \in \{\mathbf{E}, \mathbf{H}\}, \quad (14)$$

with $\mathcal{E}(k_{\mathbf{u}}) = \sum_{i=1}^{k_{\mathbf{u}}} \sigma_{\mathbf{u},i}^2 / \sum_{i=1}^{r_{\mathbf{u}}} \sigma_{\mathbf{u},i}^2$ being the relative information content and ρ being the truncation tolerance used to control the accuracy of NIMOR.

However, since time is being added as an input parameter, the snapshot matrix $\mathbb{A}_{\mathbf{u}}$ ($\mathbf{u} \in \{\mathbf{E}, \mathbf{H}\}$) has a considerable width making it very difficult and time-consuming to manipulate. So a nested POD method is employed to extract the time- and parameter-independent POD basis functions, in which the POD method is implemented separately for time and parameter spaces. The workflow of the nested POD algorithm is as follows:

(1) With a truncation tolerance ρ_t , the $k_{\mathbf{u}}^i$ POD basis $\{\phi_{\mathbf{u},j}^i\}_{j=1}^{k_{\mathbf{u}}^i}$ are obtained by using the POD method for each time-trajectory $\mathbb{A}_{\mathbf{u}}^i$ ($i = 1, 2, \dots, \mathcal{N}_p^{L+1}$, $\mathbf{u} \in \{\mathbf{E}, \mathbf{H}\}$), i.e., $\mathbb{P}_{\mathbf{u}}^i = [\phi_{\mathbf{u},1}^i, \phi_{\mathbf{u},2}^i, \dots, \phi_{\mathbf{u},k_{\mathbf{u}}^i}^i]$.

(2) Each POD basis $\mathbb{P}_{\mathbf{u}}^i$ is collected in a new time-compressed matrix $\widehat{\mathbb{A}}_{\mathbf{u}}$. With a truncation tolerance ρ_{θ} , the final $L_{\mathbf{u}}$ POD basis $\{\chi_{\mathbf{u},j}\}_{j=1}^{K_{\mathbf{u}}}$ are obtained via the POD method for the time-compressed matrix $\widehat{\mathbb{A}}_{\mathbf{u}}$, i.e., $\mathbb{P}_{\mathbf{u}} = [\chi_{\mathbf{u},1}, \chi_{\mathbf{u},2}, \dots, \chi_{\mathbf{u},L_{\mathbf{u}}}]$ ($\mathbf{u} \in \{\mathbf{E}, \mathbf{H}\}$).

The pseudo-code implementation of the nested POD method is shown in Algorithm 2.

Algorithm 2 Nested POD method

Input: Time trajectory matrices $\mathbb{A}_{\mathbf{u}}^i$ ($i = 1, 2, \dots, \mathcal{N}_p^{L+1}$, $\mathbf{u} \in \{\mathbf{E}, \mathbf{H}\}$), and truncation tolerances ρ_t and ρ_{θ}

Output: POD basis matrix $\mathbb{P}_{\mathbf{u}}$ ($\mathbf{u} \in \{\mathbf{E}, \mathbf{H}\}$)

```

1: for  $i = 1$  to  $\mathcal{N}_p^{L+1}$  do
2:    $\mathbb{P}_{\mathbf{u}}^i = \text{POD}(\mathbb{A}_{\mathbf{u}}^i, \rho_t)$ 
3: end for
4:  $\widehat{\mathbb{A}}_{\mathbf{u}} = [\mathbb{P}_{\mathbf{u}}^1, \mathbb{P}_{\mathbf{u}}^2, \dots, \mathbb{P}_{\mathbf{u}}^{\mathcal{N}_p^{L+1}}]$ 
5:  $\mathbb{P}_{\mathbf{u}} = \text{POD}(\widehat{\mathbb{A}}_{\mathbf{u}}, \rho_{\theta})$ 

6: function  $\mathbb{P} = \text{POD}(\mathbb{A}, \rho)$  do
7:    $[\mathbb{U}, \Sigma, \mathbb{V}] = \text{svd}(\mathbb{A})$ 
8:    $k = \text{argmin}\{\mathcal{E}(k) : \mathcal{E}(k) \geq 1 - \rho\}$  with  $\mathcal{E}(k)$  being the relative information content
9:    $\mathbb{P} = \mathbb{U}(:, 1 : k)$ 
10: end function

```

4. Non-intrusive reduced-order modeling

In this section, we will briefly introduce the Gaussian process regression (GPR) method and give the approximation of the reduced-order coefficients via GPR method.

4.1. Gaussian process regression

Regression is a machine learning method pertaining to the learning of a mapping function from a labeled observation set, which associates the input data with their correct continuous prediction, to its output. Unlike other parametric regression methods that only have a limited function paradigm, GPR [54, 55] is a non-parametric model based on Bayesian inference, which can not only learn any form of functions, but also directly measure the uncertainty of the prediction.

Given a set of observations $\mathcal{D} = \{(\mathbf{x}_i, y_i) : i = 1, 2, \dots, n\}$, where each p -dimensional input $\mathbf{x}_i \in \mathcal{I} \subset \mathcal{R}^p$ lies in the input domain \mathcal{I} and $y_i \in \mathcal{R}$ represents scalar output corresponding to \mathbf{x}_i (with a Gaussian noise $\epsilon \sim \mathcal{N}(0, \sigma_y^2)$), GPR assumes that all the output values obey a prior n -dimensional joint normal distribution

$$\mathbf{y}|\mathbf{X} \sim \mathcal{N}(\mathbf{0}, \mathbf{K} + \sigma_y^2 \mathbf{I}_n), \quad (15)$$

with $\mathbf{X} = [\mathbf{x}_1, \mathbf{x}_2, \dots, \mathbf{x}_n]$, $\mathbf{y} = [y_1, y_2, \dots, y_n]$, in which \mathbf{I}_n is the $n \times n$ identity matrix and \mathbf{K} is the covariance matrix with its element $K_{ij} \doteq \kappa(\mathbf{x}_i, \mathbf{x}_j)$ ($i, j = 1, 2, \dots, n$) measuring the similarity between inputs \mathbf{x}_i and \mathbf{x}_j . There is a variety of covariance functions $\kappa : \mathcal{I} \times \mathcal{I} \rightarrow \mathcal{R}$ can

be adopted to characterize \mathbf{K} , and in this work we will use the automatic *relevance determination squared exponential* function

$$\kappa(\mathbf{x}, \mathbf{x}') = \sigma_f^2 \exp\left(-\frac{1}{2} \sum_{m=1}^p \frac{(x_m - x'_m)^2}{\ell_m^2}\right), \quad \mathbf{x}, \mathbf{x}' \in \mathcal{I}, \quad (16)$$

where σ_f and ℓ_m are the signal variance and individual correlated length scale, respectively. When considering an unseen new input \mathbf{x}_* , its noise-free prediction value y_* , along with the observed outputs \mathbf{y} , will belong to another $(n + 1)$ -dimensional joint normal distribution

$$\begin{bmatrix} \mathbf{y} \\ y_* \end{bmatrix} \sim \mathcal{N}\left(\begin{bmatrix} \mathbf{0} \\ 0 \end{bmatrix}, \begin{bmatrix} \mathbf{K} + \sigma_y^2 \mathbf{I}_n & \mathbf{K}_* \\ \mathbf{K}_*^T & \mathbf{K}_{**} \end{bmatrix}\right), \quad \mathbf{K}_* = [\mathbf{K}_{*1}, \mathbf{K}_{*2}, \dots, \mathbf{K}_{*n}]^T, \quad (17)$$

based on which, the posterior probability distribution for y_* can be directly inferred using Bayes' theorem as

$$\begin{aligned} y_* | \mathbf{x}^*, \mathbf{X}, \mathbf{y} &\sim \mathcal{N}(\mu_*, \sigma_*), \\ \mu_* &= \mathbf{K}_*^T (\mathbf{K} + \sigma_y^2)^{-1} \mathbf{y}, \\ \sigma_* &= \mathbf{K}_{**} - \mathbf{K}_*^T (\mathbf{K} + \sigma_y^2)^{-1} \mathbf{K}_*. \end{aligned} \quad (18)$$

As a non-parametric model, the GPR model is uniquely determined by the covariance function and the given observation data. However, as shown in (16), the covariance function possesses hyperparameters $\boldsymbol{\mu} = \{\ell_1, \dots, \ell_p, \sigma_f, \sigma_y\}$, whose values have a great significance on the predictive performance. Since the optimal hyperparameters $\boldsymbol{\mu}_{\text{opt}}$ should maximize the conditional probability $p(\mathbf{y} | \mathbf{X}, \boldsymbol{\mu}_{\text{opt}})$, we will estimate $\boldsymbol{\mu}_{\text{opt}}$ by maximizing the following marginal log-likelihood function

$$\begin{aligned} \boldsymbol{\mu}_{\text{opt}} &= \arg \max_{\boldsymbol{\mu}} (p(\mathbf{y} | \mathbf{X}, \boldsymbol{\mu}_{\text{opt}})) \\ &= \arg \max_{\boldsymbol{\mu}} \left\{ -\frac{1}{2} (\mathbf{y}^T (\mathbf{K} + \sigma_y^2)^{-1} \mathbf{y} - \frac{1}{2} \log |\mathbf{K} + \sigma_y^2| - \frac{n}{2} \log(2\pi)) \right\}. \end{aligned} \quad (19)$$

4.2. Regression of the reduced-order coefficients

In an MOR method, the reduced-order solution \mathbf{u}_h^r ($\mathbf{u} \in \{\mathbf{E}, \mathbf{H}\}$) for a certain time and parameter values $(t, \theta) \in \mathcal{T} \times \mathcal{P}$ can be understood as the projection of the high fidelity \mathbf{u}_h solution on the RB subspace $\mathcal{V}_{rb, \mathbf{u}}$, i.e.,

$$\mathbf{u}_h^r(t, \theta) = \mathbb{P}_{\mathbf{u}} \alpha_{\mathbf{u}}(t, \theta) \in \mathcal{V}_{rb, \mathbf{u}}, \quad \mathbf{u} \in \{\mathbf{E}, \mathbf{H}\}, \quad (20)$$

where $\alpha_{\mathbf{u}}(t, \theta) = \mathbb{P}_{\mathbf{u}}^T \mathbf{u}_h(t, \theta) \in \mathcal{R}^{L_{\mathbf{u}}}$ is the reduced-order or projection coefficient vector, which is usually determined by the Galerkin or Petrov-Galerkin projection method. However, the MOR method often suffers from some issues such as numerical instability and low efficiency for complex nonlinear problems [11, 14]. So, we introduce the NIROM method, in which a regression model $\boldsymbol{\varpi}_{\mathbf{u}}$ from an input vector (t, θ) of dimension $\dim(\mathcal{P}) + 1 = p + 1$ to an output vector $\alpha_{\mathbf{u}}(t, \theta)$ of dimension $L_{\mathbf{u}}$ is built in order to predict the reduced-order coefficient $\alpha_{\mathbf{u}}(t^*, \theta^*)$ for any non-trained time/parameter values $(t^*, \theta^*) \in \mathcal{T} \times \mathcal{P}$

$$\boldsymbol{\varpi}_{\mathbf{u}} : (t, \theta) \rightarrow \alpha_{\mathbf{u}}(t, \theta), \quad \mathbf{u} \in \{\mathbf{E}, \mathbf{H}\}. \quad (21)$$

In this study, we use the GPR method to construct the regression model, acting as an approximation map $\widehat{\boldsymbol{\varpi}}_{\mathbf{u}}$ of the ideal map $\boldsymbol{\varpi}_{\mathbf{u}}$ with the following training set

$$\mathcal{D}_{\mathbf{u}, tr} = \{ \{(t, \theta), \alpha_{\mathbf{u}}(t, \theta)\} : t \in \mathcal{T}_{tr}, \theta \in \mathcal{P}_{tr}(L + 1, p)\}, \quad \mathbf{u} \in \{\mathbf{E}, \mathbf{H}\}. \quad (22)$$

Then, the reduced-order coefficients for any non-trained time and material parameter $(t^*, \theta^*) \in \mathcal{T} \times \mathcal{P}$ can be rapidly recovered without having to access to the original high-dimensional dynamical system

$$\widehat{\alpha}_{\mathbf{u}}(t^*, \theta^*) = \widehat{\varpi}_{\mathbf{u}}(t^*, \theta^*), \quad \mathbf{u} \in \{\mathbf{E}, \mathbf{H}\}, \quad (23)$$

and the corresponding reduced-order solution can be written as

$$\underline{\mathbf{u}}_h^r(t^*, \theta^*) \approx \mathbb{P}_{\mathbf{u}} \widehat{\alpha}_{\mathbf{u}}(t^*, \theta^*), \quad \mathbf{u} \in \{\mathbf{E}, \mathbf{H}\}. \quad (24)$$

In general, the reduced-order coefficients $\alpha_{\mathbf{u}}(t, \theta)$ vary more drastically with the material parameter than with time for parameterized electromagnetic scattering problems, which usually leads to a difficult global GPR model. Therefore, to ensure the reliability and effectiveness of the NIMOR method, we use the SVD method to extract the principal components of the training dataset, and then use the GPR method to approximate the dominating discrete time and material parameter modes. For the l -th component $\alpha_{\mathbf{u},l}(t, \theta)$ ($\mathbf{u} \in \{\mathbf{E}, \mathbf{H}\}$) of the reduced-order coefficient vector $\alpha_{\mathbf{u}}(t, \theta)$, the training set can be written in the following matrix form

$$\mathbb{Q}_{\mathbf{u}}^l = \begin{pmatrix} \alpha_{\mathbf{u},l}(t^{(n_1)}, \theta^{(1)}) & \alpha_{\mathbf{u},l}(t^{(n_1)}, \theta^{(2)}) & \cdots & \alpha_{\mathbf{u},l}(t^{(n_1)}, \theta^{(\mathcal{N}_p^{L+1})}) \\ \alpha_{\mathbf{u},l}(t^{(n_2)}, \theta^{(1)}) & \alpha_{\mathbf{u},l}(t^{(n_2)}, \theta^{(2)}) & \cdots & \alpha_{\mathbf{u},l}(t^{(n_2)}, \theta^{(\mathcal{N}_p^{L+1})}) \\ \vdots & \vdots & \cdots & \vdots \\ \alpha_{\mathbf{u},l}(t^{(n_{\mathcal{N}_t})}, \theta^{(1)}) & \alpha_{\mathbf{u},l}(t^{(n_{\mathcal{N}_t})}, \theta^{(2)}) & \cdots & \alpha_{\mathbf{u},l}(t^{(n_{\mathcal{N}_t})}, \theta^{(\mathcal{N}_p^{L+1})}) \end{pmatrix}, \quad l = 1, 2, \dots, L_{\mathbf{u}}.$$

By using SVD for $\mathbb{Q}_{\mathbf{u},l}$, one can obtain several discrete time- and material parameter-modes

$$\mathbb{Q}_{\mathbf{u}}^l \approx \widetilde{\mathbb{Q}}_{\mathbf{u}}^l = \sum_{j=1}^{q_{\mathbf{u}}^l} \tau_{\mathbf{u},j}^l \eta_{\mathbf{u},j}^l (\zeta_{\mathbf{u},j}^l)^T, \quad \mathbf{u} \in \{\mathbf{E}, \mathbf{H}\}, \quad (25)$$

where $\eta_{\mathbf{u},j}^l$ and $\zeta_{\mathbf{u},j}^l$ respectively are the j -th discrete time- and material parameter-modes for the l -th component of reduced-order coefficient, $\tau_{\mathbf{u},1}^l \geq \tau_{\mathbf{u},2}^l \cdots \geq \tau_{\mathbf{u},q_{\mathbf{u}}^l}^l$ are the first $q_{\mathbf{u}}^l$ singular values of matrix $\mathbb{Q}_{\mathbf{u}}^l$, and $q_{\mathbf{u}}^l$ is the truncation rank obtained by (14) with the truncation tolerance ρ_{tol}^l . By using GPR method, one can then get the corresponding continuous time- and material parameter-modes

$$\begin{cases} \{(t^{(n_i)}, (\eta_{\mathbf{u},j}^l)_i) : i = 1, 2, \dots, \mathcal{N}_t\} & \xrightarrow{\text{GPR method}} \bar{\eta}_{\mathbf{u},j}^l(t), \\ \{(\theta^{(i)}, (\zeta_{\mathbf{u},j}^l)_i) : i = 1, 2, \dots, \mathcal{N}_p^{L+1}\} & \xrightarrow{\text{GPR method}} \bar{\zeta}_{\mathbf{u},j}^l(t), \end{cases} \quad (26)$$

where $\bar{\eta}_{\mathbf{u},j}^l$ and $\bar{\zeta}_{\mathbf{u},j}^l$ respectively are the j -th continuous time- and parameter-modes for the l -th component of reduced-order coefficient. For the new time and material parameter $(t^*, \theta^*) \in \mathcal{T} \times \mathcal{P}$, the l -th component $\alpha_{\mathbf{u},l}(t, \theta)$ can be rapidly recovered as

$$\begin{aligned} \alpha_{\mathbf{u},l}(t^*, \theta^*) &\approx \widehat{\alpha}_{\mathbf{u},l}(t^*, \theta^*) \\ &\approx \bar{\alpha}_{\mathbf{u},l}(t^*, \theta^*) \\ &= \sum_{j=1}^{q_{\mathbf{u}}^l} \tau_{\mathbf{u},j}^l \bar{\eta}_{\mathbf{u},j}^l(t^*) (\bar{\zeta}_{\mathbf{u},j}^l(\theta^*))^T, \quad l = 1, 2, \dots, L_{\mathbf{u}}, \quad \mathbf{u} \in \{\mathbf{E}, \mathbf{H}\}. \end{aligned} \quad (27)$$

Finally, one can obtain the reduced-order solution $\underline{\mathbf{u}}_h^r(t^*, \theta^*)$ via (20). The process of NIMOR with the offline/online stages proposed in this paper is shown in Algorithm 3, in which the offline and online stages of the GPR-based NIMOR are decoupled.

Algorithm 3 GPR-based NIMOR for parameterized time-domain Maxwell's equations

Offline stage
a) Construction of POD basis functions

1. Choice of training sets $\mathcal{P}_{tr}(L, p)$ and $\mathcal{P}_{tr}(L+1, p)$ with $\mathcal{P}_{tr}(L, p) \subset \mathcal{P}_{tr}(L+1, p)$ ($L \geq 1$)
2. Obtain snapshot vectors in $\mathcal{P}_{tr}(L, p)$ via DGTD method
3. Interpolation of snapshot vector in $\mathcal{P}_{tr}(L+1, p)$ via **Algorithm 1**
4. Compute POD basis function $\mathbb{P}_{\mathbf{u}}$ ($\mathbf{u} \in \{\mathbf{E}, \mathbf{H}\}$) via **Algorithm 2**

b) Construction of surrogate model

1. Compute the reduced-order coefficients $\alpha_{\mathbf{u}}(t, \theta) = \mathbb{P}_{\mathbf{u}}^T \mathbf{u}_h(t, \theta)$, $t \in \mathcal{T}_{tr}$, $\theta \in \mathcal{P}_{tr}(L+1, p)$
2. Obtain discrete time- and material parameter-modes $\eta_{\mathbf{u},j}^l$ and $\zeta_{\mathbf{u},j}^l$ by performing SVD for $\mathbb{Q}_{\mathbf{u}}^l$
3. Obtain continuous time- and parameter-models $\bar{\eta}_{\mathbf{u},j}^l$ and $\bar{\zeta}_{\mathbf{u},j}^l$ by using GPR method
4. Construct surrogate model via (27)

Online stage

1. Recover output $\bar{\alpha}_{\mathbf{u},l}(t^*, \theta^*)$ for new time and parameter value $(t^*, \theta^*) \in \mathcal{T} \times \mathcal{P}$
 2. Compute the reduced-order solution via (24) and (27)
-

5. Numerical results

In this section, some numerical results for scattering of a plane wave by a dielectric disk and by a multi-layer heterogeneous medium are presented to validate the effectiveness and the accuracy of the proposed NIMOR method. We adopt the transverse magnetic (TM) formulation of the time-domain Maxwell's equations, i.e., $\mathbf{E} = (0, 0, E_z)^T$ and $\mathbf{H} = (H_x, H_y, 0)^T$. The excitation in all scattering scenarios is a plane wave such that $E_z^{\text{inc}} = \cos(\omega t - kx)$ and $H_y^{\text{inc}} = -\cos(\omega t - kx)$ with $\omega = 2\pi f$ being the angular frequency of the incident wave frequency $f = 300$ MHz, and k being the wave number in vacuum. To evaluate the accuracy of the numerical results, the following relative projection and NIMOR errors are defined

$$\left\{ \begin{array}{l} \text{Relative projection error : } e_{\mathbf{u},\text{Pro}}(t, \theta) = \frac{\| \mathbf{u}_h(t, \theta) - \mathbb{P}_{\mathbf{u}} \mathbb{P}_{\mathbf{u}}^T \mathbf{u}_h(t, \theta) \|_{\mathcal{R}^{\mathcal{N}_d}}}{\| \mathbf{u}_h(t, \theta) \|_{\mathcal{R}^{\mathcal{N}_d}}}, \\ \text{Relative NIMOR error : } e_{\mathbf{u},\text{NIMOR}}(t, \theta) = \frac{\| \mathbf{u}_h(t, \theta) - \mathbb{P}_{\mathbf{u}} \alpha_{\mathbf{u}}(t, \theta) \|_{\mathcal{R}^{\mathcal{N}_d}}}{\| \mathbf{u}_h(t, \theta) \|_{\mathcal{R}^{\mathcal{N}_d}}}, \end{array} \right. \quad \mathbf{u} \in \{\mathbf{E}, \mathbf{H}\},$$

and the corresponding average relative errors are also defined on a testing time/parameter sampling $\mathcal{T}_{te} \times \mathcal{P}_{te}$ of size \mathcal{N}_{te}

$$\bar{e}_{\mathbf{u},\text{Pro}} = \frac{\sum_{(t,\theta) \in \mathcal{T}_{te} \times \mathcal{P}_{te}} e_{\mathbf{u},\text{Pro}}(t, \theta)}{\mathcal{N}_{te}}, \quad \bar{e}_{\mathbf{u},\text{NIMOR}} = \frac{\sum_{(t,\theta) \in \mathcal{T}_{te} \times \mathcal{P}_{te}} e_{\mathbf{u},\text{NIMOR}}(t, \theta)}{\mathcal{N}_{te}}, \quad \mathbf{u} \in \{\mathbf{E}, \mathbf{H}\},$$

where the testing parameter set \mathcal{P}_{te} is generated via randomized latin-hypercube-sampling (LHS) method, and the testing time set \mathcal{T}_{te} is randomly chosen within the last period of the physical simulation. The GPR-based approximation of reduced-order coefficient matrices are constructed via the MATLAB function `fitrgp`. The DGTD and NIMOR methods are implemented in MATLAB and simulations are run on a workstation equipped with an Intel Core i7-10700F CPU running at 2.90 GHz, and with 16 GB of RAM memory.

5.1. Scattering of plane wave by a dielectric disk

As a benchmark test, the electromagnetic scattering of a plane wave by a dielectric disk with a varying relative permittivity is considered. The radius of the disk is set to 0.6 m, and

the computational domain is the square $\Omega_{\square} = [-2.6 \text{ m}, 2.6 \text{ m}] \times [-2.6 \text{ m}, 2.6 \text{ m}]$, on which the first order Silver-Müller ABC is imposed artificially truncate the infinite domain. The interest relative permittivity of the disk ranges $\varepsilon_r \in [1, 5]$, and the relative permeability is set to $\mu_r = 1$ (nonmagnetic material), i.e., $\mathcal{P} = \{\theta : \theta = \varepsilon_r \in [1, 5]\} \subset \mathcal{R}$. The medium exterior to the dielectric disk is assumed to be vacuum.

The high-fidelity simulations in the dataset $\mathcal{P}_{tr}(5, 1)$ are performed by using a second-order DGTD solver on a triangular mesh with 2575 nodes, and 5044 elements of which 1092 elements are located inside the disk. The total simulation time is set to 50 periods (which corresponds to 50 m in normalized unit), and the time step is $\Delta t = 3.678 \times 10^{-3}$ s. For each selected training parameter, the snapshot vectors are chosen every time step within the last period, i.e., $\mathcal{T}_{tr} = \{49.0024, 49.006, \dots, 49.9623, 49.966\}$, and the number of time points is $\mathcal{N}_t = 263$.

In order to assess the numerical accuracy of the NIMOR method proposed here (termed as NIMOR⁽¹⁾ method, where the snapshot vectors in the training set $\mathcal{P}_{tr}(6, 1)$ are constructed via **Algorithm 1** whose time cost is very low), a traditional NIMOR method (termed as NIMOR⁽²⁾ method, where the snapshot vectors in the training set $\mathcal{P}_{tr}(6, 1)$ are directly constructed via DGTD method, which is very time consuming) is also implemented.

Figure 3 shows the numerical convergence of the NIMOR⁽¹⁾ and NIMOR⁽²⁾ methods on the testing set $\mathcal{T}_{te} \times \mathcal{P}_{te}$ in which the truncation tolerance $\rho_t = 1 \times 10^{-1}$, the size of the testing parameter set \mathcal{P}_{te} is 40, and the testing time set $\mathcal{T}_{te} = \mathcal{T}_{tr}$. The details for the training and

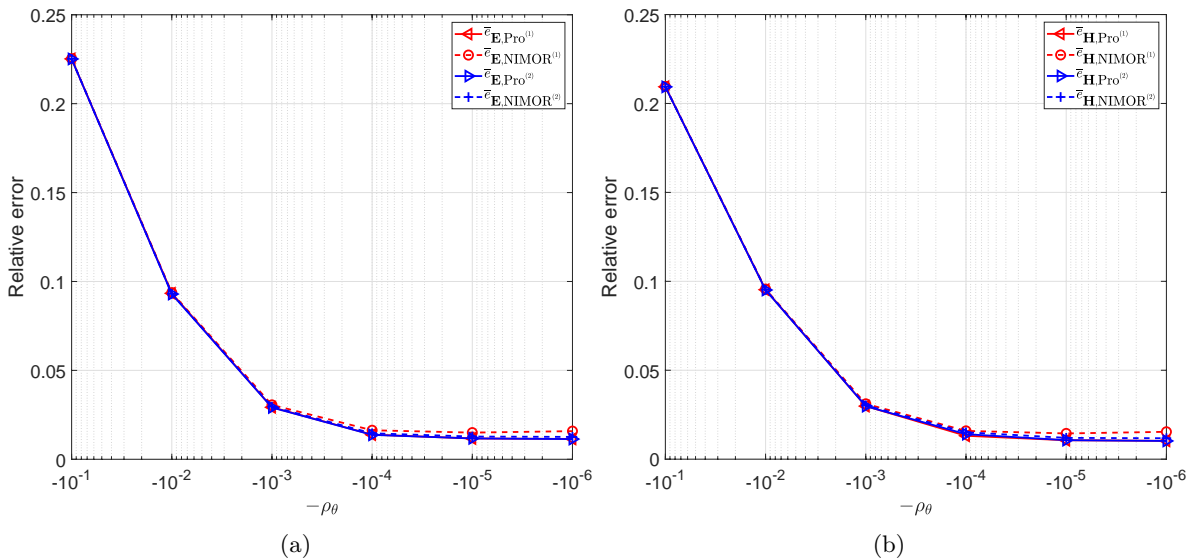


Figure 3: Scattering of plane wave by a dielectric disk: the convergence histories of $\bar{e}_{\mathbf{E},\text{Pro}^{(i)}}$, and $\bar{e}_{\mathbf{E},\text{NIMOR}^{(i)}}$ (a), $\bar{e}_{\mathbf{H},\text{Pro}^{(i)}}$, and $\bar{e}_{\mathbf{H},\text{NIMOR}^{(i)}}$ (b) ($i = 1, 2$) on the testing set $\mathcal{T}_{te} \times \mathcal{P}_{te}$ with vary truncation tolerances ρ_θ , where $\bar{e}_{\mathbf{u},\text{Pro}^{(i)}}$ is the average projection error of NIMOR⁽ⁱ⁾ method for \mathbf{u} .

testing datasets are listed in Table 2. It can be seen from Figure 3 that the NIMOR⁽¹⁾ method

Table 2: Scattering of plane wave by a dielectric disk: settings for the training, and testing datasets.

Data set	Training set	Testing set
Parameter sample points	65, uneven (Smolyak mehod)	40, random (LHS method)
Time sample points	263, uniform	263, uniform
Size	17095	10520

has almost the same accuracy as the NIMOR⁽²⁾ method, i.e., NIMOR⁽¹⁾ can still achieve high

accuracy with a small number high-fidelity simulations. From Figure 3, we select the error bounds $\rho_t = 1 \times 10^{-1}$ and $\rho_\theta = 1 \times 10^{-5}$ in the NIMOR⁽¹⁾ and NIMOR⁽²⁾ methods, which results in a set of $L_{E_z} = 23$, $L_{H_x} = 91$, $L_{H_y} = 22$, and $L_{E_z} = 22$, $L_{H_x} = 75$, $L_{H_y} = 21$ POD basis functions, respectively. The corresponding projection and NIMOR⁽ⁱ⁾ ($i = 1, 2$) errors are shown in Table 3. Some of the exact reduced-order coefficients of E_z and H_y , and the corresponding

Table 3: Scattering of plane wave by a dielectric disk: the average projection and NIMOR errors on the testing set.

Average relative errors	$\bar{e}_{\mathbf{E},\text{Pro}}$	$\bar{e}_{\mathbf{E},\text{NIMOR}}$	$\bar{e}_{\mathbf{H},\text{Pro}}$	$\bar{e}_{\mathbf{H},\text{NIMOR}}$
NIMOR ⁽¹⁾ method	1.170×10^{-2}	1.500×10^{-2}	1.065×10^{-2}	1.447×10^{-2}
NIMOR ⁽²⁾ method	1.173×10^{-2}	1.279×10^{-2}	1.069×10^{-2}	1.198×10^{-2}

approximation reduced-order coefficients based on NIMOR⁽¹⁾ method are shown in Figures 4 and Figures 5. The SVD truncation criterions for all reduced-order coefficient matrices are set to $\rho_{l,\text{tol}} = 1 \times 10^{-4}$ for $1 \leq l \leq 5$, $\rho_{l,\text{tol}} = 5 \times 10^{-4}$ for $6 \leq l \leq 10$, $\rho_{l,\text{tol}} = 1 \times 10^{-3}$ for $11 \leq l \leq 20$, and $\rho_{l,\text{tol}} = 5 \times 10^{-3}$ for $21 \leq l \leq L_{\mathbf{u}}$ ($\mathbf{u} = \mathbf{E}, \mathbf{H}$). Smaller values of the truncation criterions are defined for the above coefficients since they play a dominant role in the accuracy of the reduced-order solutions. In particular, the GPR-based approximation models $\bar{\alpha}_{\mathbf{u},l}(t, \theta)$ ($l = 1, 2, \dots, L_{\mathbf{u}}$) can be stored in the offline stage, and for new time and parameter, one can directly call these models to compute the electromagnetic fields in the online stage. After the

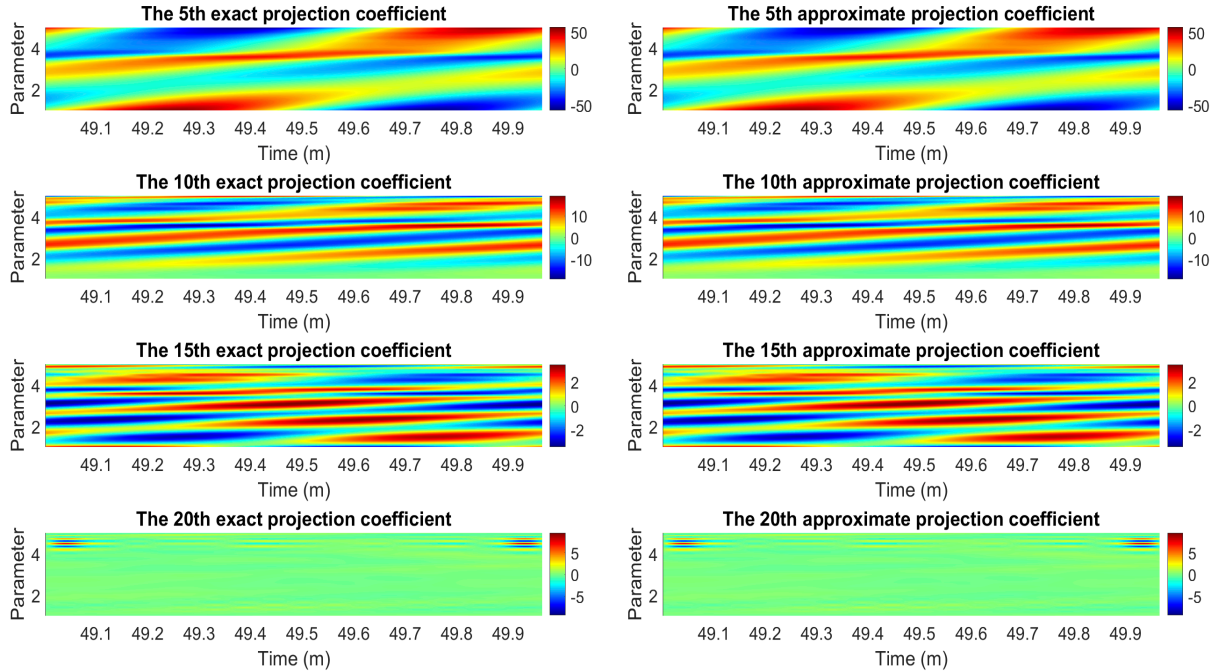


Figure 4: Scattering of plane wave by a dielectric disk: the 5-th, 10-th, 15-th, and 20-th exact and approximation reduced-order coefficients of E_z based on NIMOR⁽¹⁾.

offline stage, in order to verify the performance of NIMOR method built here, the online tests are performed on the solutions for testing parameters, and chosen as $\theta^{(1)} = 1.215$, $\theta^{(2)} = 2.215$, $\theta^{(3)} = 3.215$ and $\theta^{(4)} = 4.215$. The 1-D x-wise distribution of the real part of E_z and H_y in the Fourier domain over the last period of simulation along $y = 0$ is displayed in Figure 6. The time evolution of relative projection and NIMOR errors for the testing parameters are shown

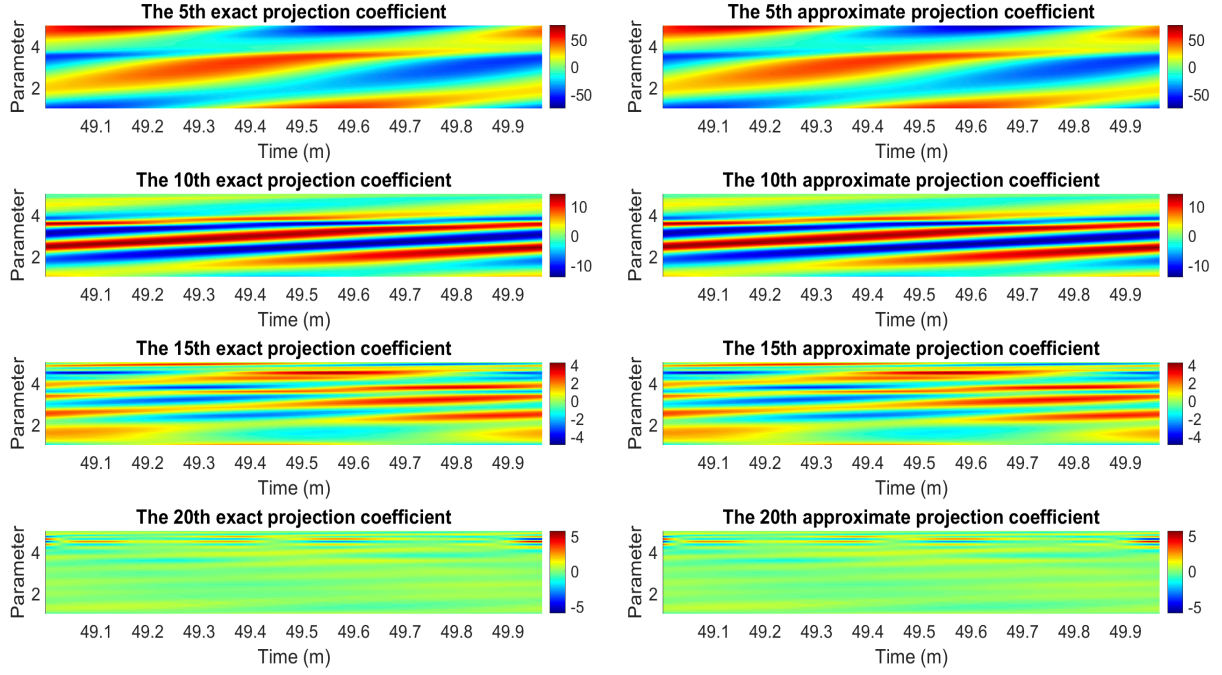


Figure 5: Scattering of plane wave by a dielectric disk: the 5-th, 10-th, 15-th, and 20-th exact and approximation reduced-order coefficients of H_y based on NIMOR⁽¹⁾.

in Figure 7. Finally, the computational times of NIMOR⁽ⁱ⁾ ($i = 1, 2$) and DGTD methods are reported in Table 4, where we record the offline computing time of NIMOR⁽ⁱ⁾ ($i = 1, 2$) method including the generation of snapshot vectors, the construction of POD basis functions and the approximation of reduced coefficient matrices based on the GPR method, as well as the computing time of DGTD solver and NIMOR⁽ⁱ⁾ ($i = 1, 2$) online for new parameter. The results in Table 4 indicate that the offline computing time of the NIMOR⁽¹⁾ method based the RBF method is smaller than that of NIMOR⁽²⁾ method, in which most of the offline cost is due to the generation of snapshot vectors. Moreover, the online time of NIMOR⁽ⁱ⁾ ($i = 1, 2$) is greatly shortened compared with the DGTD method for a new parameter, which demonstrates the efficiency of NIMOR method. For this problem, we can conclude that the NIMOR method proposed in this study is effective for the parameterized time-domain Maxwell's equations.

Table 4: Scattering of plane wave by a dielectric disk: computational times of NIMOR⁽ⁱ⁾ ($i = 1, 2$) and DGTD methods in terms of CPU time. The unit of time cost is second.

Method	Offlin stage (Snapshots, Nested POD, GRP training)	Online stage (one run for new paramter)
DGTD	-	4.254×10^2
NIMOR ⁽¹⁾	1.444×10^4	3.8
NIMOR ⁽²⁾	2.793×10^4	3.1

5.2. Scattering of plane wave by a multi-layer heterogeneous medium

Next, we consider a multivariate problem, which is induced by a multilayer heterogeneous medium, as shown in Figure 8. This multilayer heterogeneous medium is again illuminated by an incident plane wave. Table 5 summarizes the radius of each medium layer and the corresponding relative permittivity range. The computational domain is artificially truncated

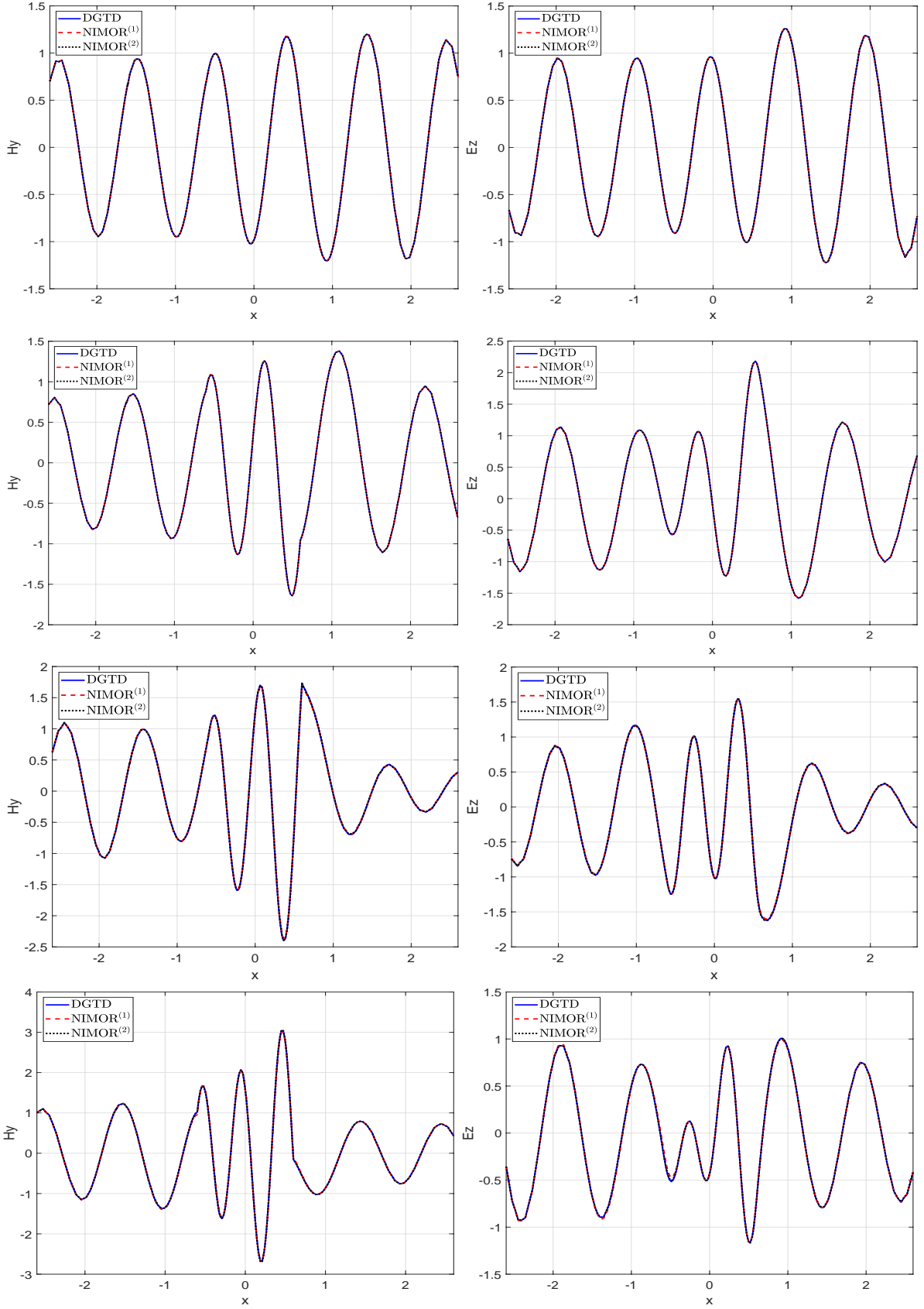


Figure 6: Scattering of plane wave by a dielectric disk: comparison of the 1-D x -wise distribution along $y = 0$ of the real part of H_y (left) and E_z (right) of four test points: $\theta^{(1)} = 1.215$ (1-th row), $\theta^{(2)} = 2.215$ (2-th row), $\theta^{(3)} = 3.215$ (3-th row) and $\theta^{(4)} = 4.215$ (4-th row).

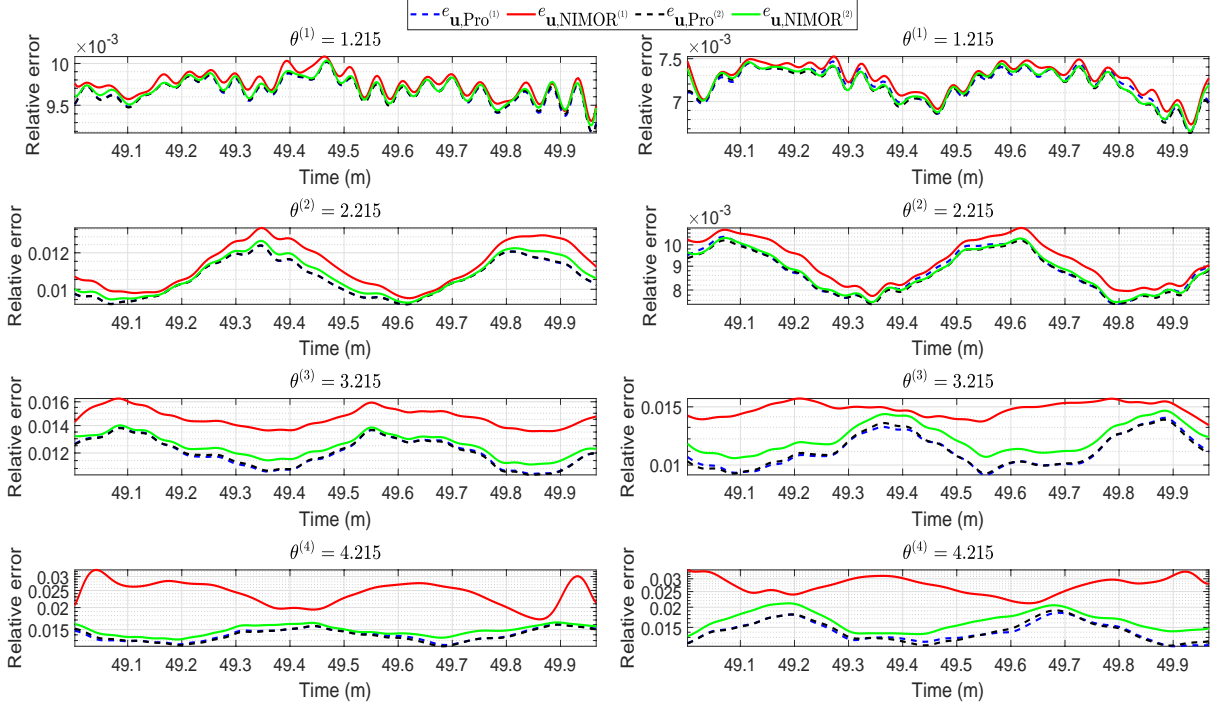


Figure 7: Scattering of plane wave by a dielectric disk: comparison of relative projection and NIMOR errors for \mathbf{E} (left) and \mathbf{H} (right) four the testing parameters.

by a square with 6.4 m side length, on which the Silver-Müller ABC condition be enforced on its boundary. The external domain of the multilayer medium is vacuum, i.e., $\varepsilon_{r,5} = \mu_{r,5} = 1$. So, the material parameters can be cast in a 4-dimensional vector $\theta = (\varepsilon_{r,1}, \varepsilon_{r,2}, \varepsilon_{r,3}, \varepsilon_{r,4}) \in \mathcal{P} = \mathcal{P}^{(1)} \times \mathcal{P}^{(2)} \times \mathcal{P}^{(3)} \times \mathcal{P}^{(4)}$. In the offline stage, the high-fidelity simulations in the training

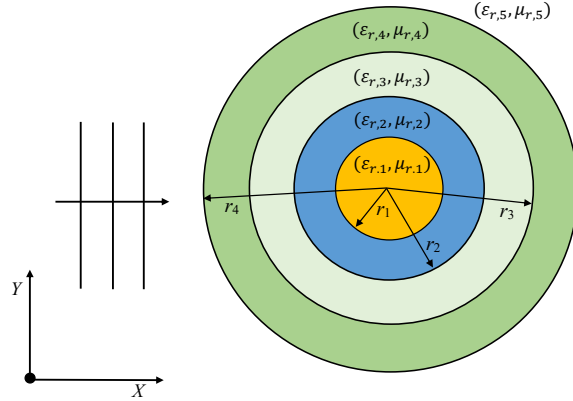


Figure 8: Scattering of a plane wave by a multi-layer heterogeneous medium: geometry of the multi-layer medium.

dataset $\mathcal{P}_{tr}(2, 4)$ chosen using the Smolyak grid method are performed using the DGTD solver with a second order polynomial approximation on a triangular mesh with 2049 nodes and 4016 elements until $T_f = 50$ m. The time step is $\Delta = 3.800 \times 10^{-3}$ m. $\mathcal{N}_t = 253$ snapshot vectors are obtained at regularly spaced time intervals during the last period from the high fidelity solutions for each selected parameter point $\theta \in \mathcal{P}_{tr}(2, 4)$. All of the snapshot vectors in the training dataset $\mathcal{P}_{tr}(3, 4) \setminus \mathcal{P}_{tr}(2, 4)$ are then constructed via **Algorithm 1** (termed as NIMOR⁽¹⁾ method). Similar to 5.1 section, the NIMOR⁽²⁾ method is also implemented to

Table 5: Scattering of a plane wave by a multi-layer heterogeneous medium: the distribution and range of material parameters.

Layer i	$\mathcal{P}^{(i)}$	$\mu_{r,i}$	r_i
1	$\varepsilon_{r,1} \in [5.0, 5.6]$	1	0.15
2	$\varepsilon_{r,2} \in [3.25, 3.75]$	1	0.3
3	$\varepsilon_{r,3} \in [2.0, 2.5]$	1	0.45
4	$\varepsilon_{r,4} \in [1.25, 1.75]$	1	0.6

evaluate the accuracy of the NIMOR method proposed in this study.

As with the previous problem, the numerical convergence of the NIMOR⁽¹⁾ and NIMOR⁽²⁾ methods on the testing set $\mathcal{T}_{te} \times \mathcal{P}_{te}$ is shown in Figure 9, where the truncation tolerance $\rho_t = 1 \times 10^{-1}$, the size of the testing parameter set \mathcal{P}_{te} is 40, and the testing time set $\mathcal{T}_{te} = \mathcal{T}_{tr}$. The corresponding training and testing parameter sets are listed in Table 6. We can obtain a conclusion similar to Figure 3 from Figure 9. In this test, the truncation errors for the

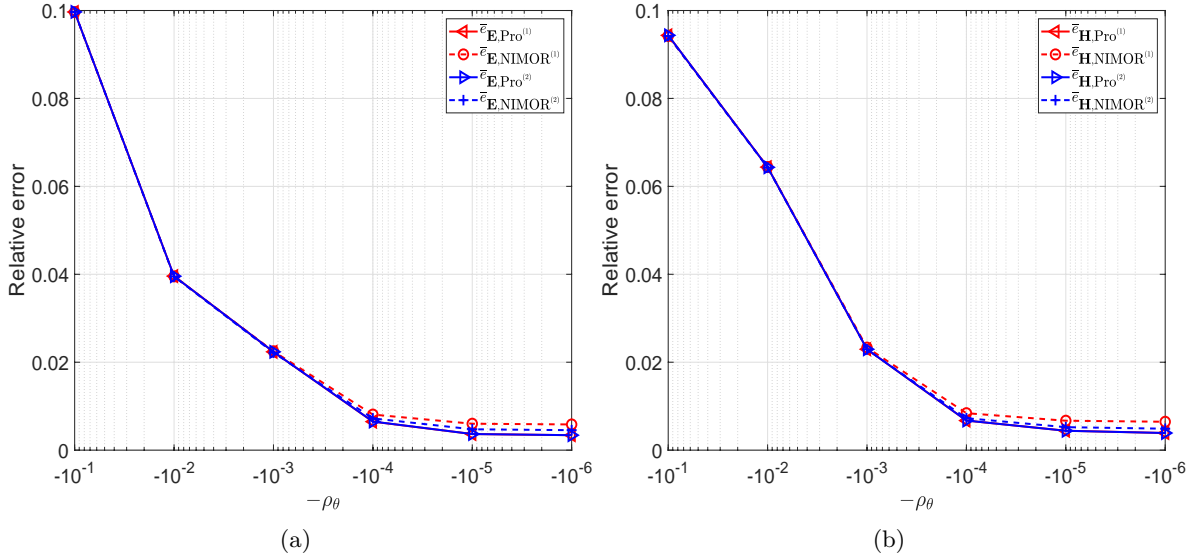


Figure 9: Scattering of a plane wave by a multi-layer heterogeneous medium: the convergence histories of $\bar{e}_{\mathbf{E},\text{Pro}^{(i)}}$, and $\bar{e}_{\mathbf{E},\text{NIMOR}^{(i)}}$ (a), $\bar{e}_{\mathbf{H},\text{Pro}^{(i)}}$, and $\bar{e}_{\mathbf{H},\text{NIMOR}^{(i)}}$ (b) ($i = 1, 2$) on the testing set $\mathcal{T}_{te} \times \mathcal{P}_{te}$ with vary truncation tolerances ρ_θ , where $\bar{e}_{\mathbf{u},\text{Pro}^{(i)}}$ is the average projection error of NIMOR⁽ⁱ⁾ method for \mathbf{u} .

Table 6: Scattering of plane wave by a multi-layer heterogeneous medium: settings for the training, and testing datasets.

Data set	Training set	Testing set
Parameter sample points	137, uneven (Smolyak method)	40, random (LHS method)
Time sample points	253, uniform	253, uniform
Size	34661	10120

nested POD method are $\rho_t = 1 \times 10^{-1}$ and $\rho_\theta = 1 \times 10^{-5}$, which results in a set of $L_{E_z} = 15$, $L_{H_x} = 16$, and $L_{H_y} = 15$ reduced basis functions. The corresponding projection and NIMOR⁽ⁱ⁾ ($i = 1, 2$) errors are presented in Table 7. Once the SVD of all projection coefficients matrices is computed, the global approximation reduced-order coefficients for new time/parameter values are constructed as the combination of time- and parameter-modes obtained by GPR method,

Table 7: Scattering of plane wave by a multi-layer heterogeneous medium: the average projection and NIMOR errors on the testing set.

Average relative errors	$\bar{\epsilon}_{\mathbf{E},\text{Pro}}$	$\bar{\epsilon}_{\mathbf{E},\text{NIMOR}}$	$\bar{\epsilon}_{\mathbf{H},\text{Pro}}$	$\bar{\epsilon}_{\mathbf{H},\text{NIMOR}}$
NIMOR ⁽¹⁾ method	3.668×10^{-3}	6.011×10^{-3}	4.419×10^{-3}	6.695×10^{-3}
NIMOR ⁽²⁾ method	3.665×10^{-3}	4.744×10^{-3}	4.405×10^{-3}	5.229×10^{-3}

and some of the approximation time-models for E_z and H_y are shown in Figure 10, where the corresponding exact time-models are also shown. Similarly, the SVD truncation tolerances are set to $\rho_{l,\text{tol}} = 5 \times 10^{-5}$ for $1 \leq l \leq 5$, $\rho_{l,\text{tol}} = 1 \times 10^{-4}$ for $6 \leq l \leq 10$, $\rho_{l,\text{tol}} = 5 \times 10^{-4}$ for $11 \leq l \leq 20$ and $\rho_{l,\text{tol}} = 1 \times 10^{-3}$ for $21 \leq l \leq L_{\mathbf{u}}$ ($\mathbf{u} = \mathbf{E}, \mathbf{H}$) for the training of GPR models. After the offline training, online tests are performed for four non-trained

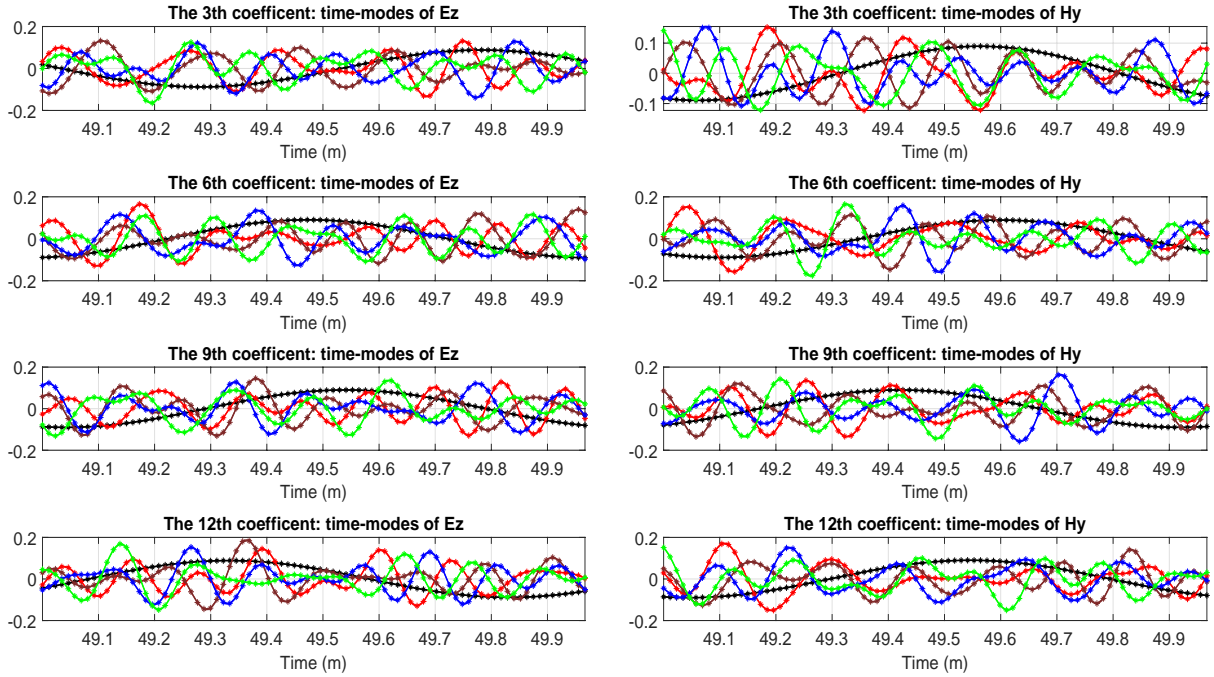


Figure 10: Scattering of plane wave by a multi-layer heterogeneous medium: the 3th, 6th, 9th, and 12th exact (—) and approximation (*) time-modes for E_z (left) and H_y (right) (the 1th mode: black, the 3th mode: red, the 5th mode: brown; the 7th mode: blue; the 9th mode: green).

parameters θ chosen as $\theta^{(1)} = \{(5.125, 3.375, 2.125, 1.375)\}$, $\theta^{(2)} = \{(5.425, 3.625, 2.425, 1.625)\}$, $\theta^{(3)} = \{(5.125, 3.625, 2.125, 1.625)\}$, and $\theta^{(4)} = \{(5.425, 3.375, 2.425, 1.375)\}$. An illustration of the efficiency of the NIMOR⁽¹⁾ method is given in Figure 11, which presents the 1-D x-wise distributions of the real part of H_y and E_z in the Fourier domain over the last period of simulation along $y = 0$ based on the NIMOR⁽¹⁾, NIMOR⁽²⁾, and DGTD method, demonstrating a fine matching between DGTD solutions and reduced-order solutions. Moreover, the time evolution of the relative projection and total errors between NIMOR⁽ⁱ⁾ ($i = 1, 2$) and DGTD are exhibited in Figure 12. Finally, the performance results obtained by the NIMOR⁽ⁱ⁾ ($i = 1, 2$) and DGTD methods with second order polynomial approximation are summarized in Table 8. We find that the NIMOR⁽²⁾ method spends 4.221×10^4 s on the offline stage, while the NIMOR⁽²⁾ method with RBF method only spends 1.912×10^4 s on the offline stage. Moreover, the NIMOR⁽¹⁾ and NIMOR⁽²⁾ methods only spend 3.9 s and 3.3 s on the online stage for new

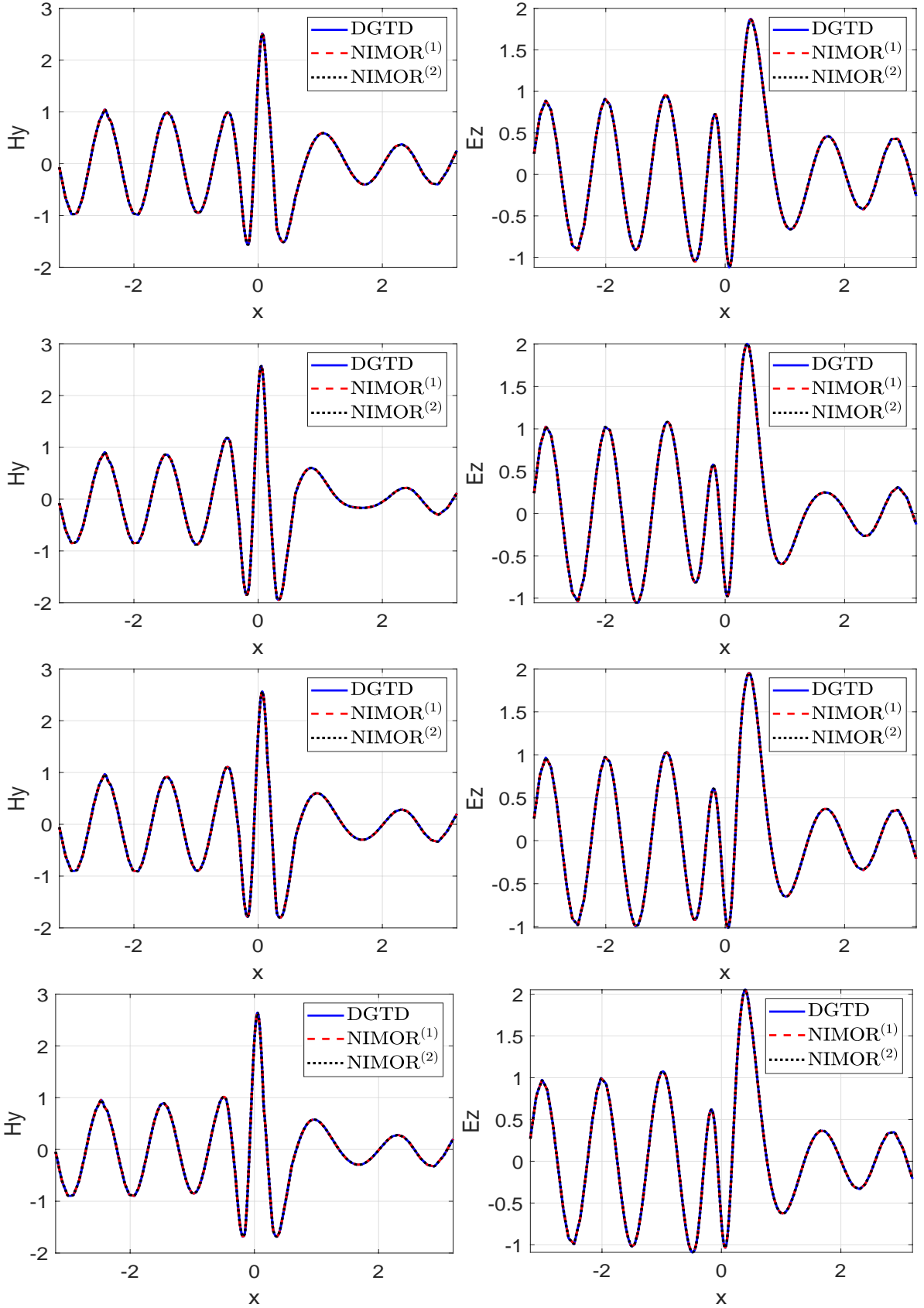


Figure 11: Scattering of plane wave by a multi-layer heterogeneous medium: comparison of the 1-D x-wise distribution along $y = 0$ of the real part of H_y (left) and E_z (right) of four test points: $\theta^{(1)} = \{(5.125, 3.375, 2.125, 1.375)\}$ (1-th row), $\theta^{(2)} = \{(5.425, 3.625, 2.425, 1.625)\}$ (2-th row), $\theta^{(3)} = \{(5.125, 3.625, 2.125, 1.625)\}$ (3-th row) and $\theta^{(4)} = \{(5.425, 3.375, 2.425, 1.375)\}$ (4-th row).

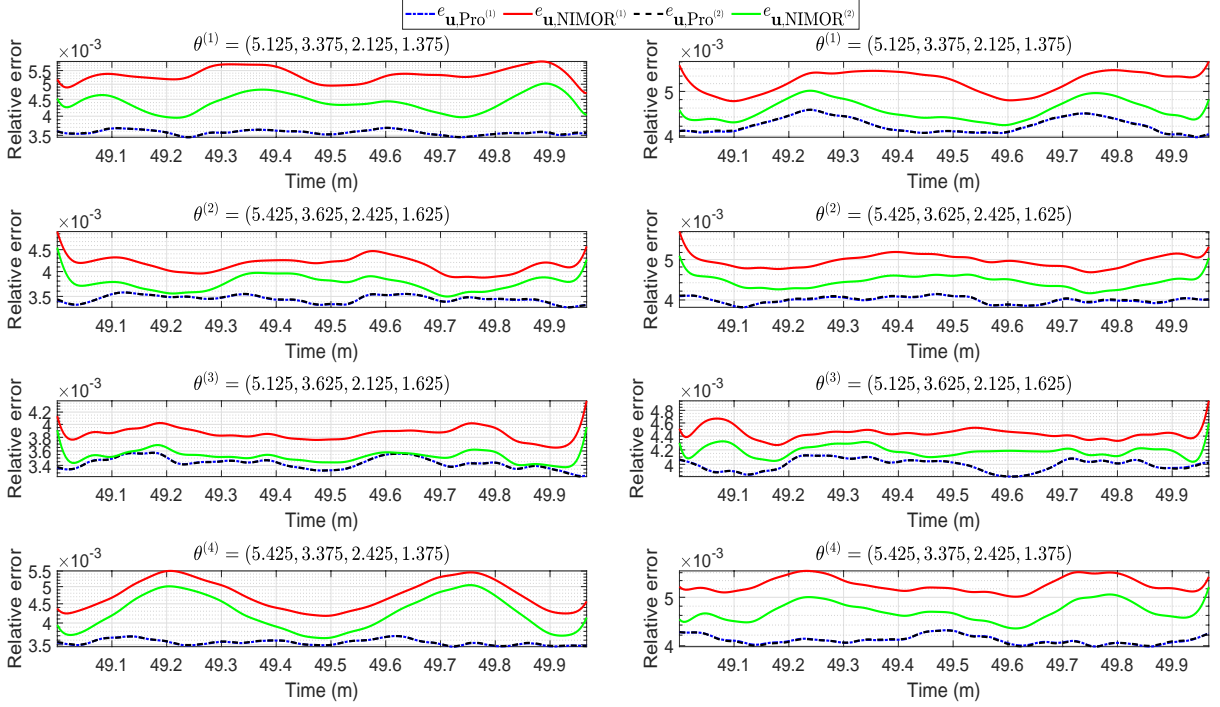


Figure 12: Scattering of plane wave by a multi-layer heterogeneous medium: comparison of relative projection and NIMOR errors for \mathbf{E} (left) and \mathbf{H} (right) four the testing parameters.

time/parameter, respectively. So, the NIMOR⁽¹⁾ method proposed here is effective for the parameterized time-domain Maxwell's equations.

Table 8: Scattering of plane wave by a multi-layer heterogeneous medium: computational times of NIMOR⁽ⁱ⁾ ($i = 1, 2$) and DGTD methods in terms of CPU time. The unit of time cost is second.

Method	Offlin stage (Snapshots, Nested POD, GRP training)	Online stage (one run for new paramter)
DGTD	-	4.513×10^2
NIMOR ⁽¹⁾	1.912×10^4	3.9
NIMOR ⁽²⁾	4.221×10^4	3.3

6. Conclusion

In this paper, we have proposed and studied a non-intrusive model order reduction method for the parameterized time-domain Maxwell's equations. Few snapshot vectors are first generated from the high-fidelity DGTD solver at the Smolyak sparse grid with approximation level L ($L \geq 1$), and then more snapshot vectors at the Smolyak sparse grid with approximation level $L + 1$ are constructed to improve the accuracy of the NIMOR method. The reduced basis functions are extracted from the chosen snapshot vectors via a nested proper orthogonal decomposition method, and the reduced coefficients are approximated by a Gaussian process regression method, in which the dominating time- and parameter modes of the reduced coefficient matrices are approximated to ensure the reliability and effectiveness of NIMOR method. The offline stage consists of the computation of the POD basis functions and the regression of the reduced coefficients, while the online stage only performs evaluation of the GPR method

and linear combination of the POD basis functions. Numerical experiments for the scattering of a plane wave by a 2-D dielectric cylinder and a multi-layer heterogeneous medium nicely illustrate the performance of the proposed NIMOR method. In the near future, we will consider more complex 3-D realistic applications and the reduction of parameterized geometry.

Declarations

Fundings

This research was supported by the NSFC (Grant No. 61772003 and 12101511), and the Key Projects of Applied Basic Research in Sichuan Province (Grant No. 2020YJ0216).

Conflicts of interest/Competing interests

We declare that we have no financial and personal relationships with other people or organizations that can inappropriately influence our work, there is no professional or other personal interest of any nature or kind in any product, service and/or company that could be construed as influencing the position presented in, or the review of, the manuscript entitled.

Availability of data and material

Not applicable

Code availability

Not applicable

References

- [1] J. S. Hesthaven, T. Warburton, Nodal discontinuous Galerkin methods: algorithms, analysis, and applications, Springer Science & Business Media, 2007.
- [2] J. Viquerat, S. Lanteri, Simulation of near-field plasmonic interactions with a local approximation order discontinuous Galerkin time-domain method, *Photonics and Nanostructures-Fundamentals and Applications* 18 (2016) 43–58.
- [3] N. Schmitt, C. Scheid, J. Viquerat, S. Lanteri, Simulation of three-dimensional nanoscale light interaction with spatially dispersive metals using a high order curvilinear DGTD method, *Journal of Computational Physics* 373 (2018) 210–229.
- [4] M. Bernacki, L. Fezoui, S. Lanteri, S. Piperno, Parallel discontinuous Galerkin unstructured mesh solvers for the calculation of three-dimensional wave propagation problems, *Applied Mathematical Modelling* 30 (8) (2006) 744–763.
- [5] P. Benner, S. Gugercin, K. Willcox, A survey of projection-based model reduction methods for parametric dynamical systems, *SIAM Review* 57 (4) (2015) 483–531.
- [6] J. S. Hesthaven, G. Rozza, B. Stamm, et al., *Certified reduced basis methods for parametrized partial differential equations*, Springer, 2016.
- [7] B. Peherstorfer, K. Willcox, M. Gunzburger, Survey of multifidelity methods in uncertainty propagation, inference, and optimization, *SIAM Review* 60 (3) (2018) 550–591.
- [8] F. Vidal-Codina, N. C. Nguyen, J. Peraire, Computing parametrized solutions for plasmonic nanogap structures, *Journal of Computational Physics* 366 (2018) 89–106.

- [9] K. Li, T.-Z. Huang, L. Li, S. Lanteri, Non-intrusive reduced-order modeling of parameterized electromagnetic scattering problems using cubic spline interpolation, *Journal of Scientific Computing* 87 (2) (2021). doi:<https://doi.org/10.1007/s10915-021-01467-2>.
- [10] M. Guo, J. S. Hesthaven, Data-driven reduced order modeling for time-dependent problems, *Computer Methods in Applied Mechanics and Engineering* 345 (2019) 75–99.
- [11] Q. Wang, J. S. Hesthaven, D. Ray, Non-intrusive reduced order modeling of unsteady flows using artificial neural networks with application to a combustion problem, *Journal of Computational Physics* 384 (2019) 289–307.
- [12] J. S. Hesthaven, U. Stefano, Non-intrusive reduced order modeling of nonlinear problems using neural networks, *Journal of Computational Physics* 363 (2018) 55–78.
- [13] S. L. Lohr, *Sampling: design and analysis*, Toronto, Canada: Nelson Education, 2009.
- [14] D. Xiao, F. Fang, C. Pain, I. Navon, A parameterized non-intrusive reduced order model and error analysis for general time-dependent nonlinear partial differential equations and its applications, *Computer Methods in Applied Mechanics and Engineering* 317 (2017) 868–889.
- [15] D. Xiao, Z. Lin, F. Fang, C. C. Pain, L. M. Navon, P. Salinas, A. Muggeridge, Non-intrusive reduced-order modeling for multiphase porous media flows using smolyak sparse grids, *International Journal for Numerical Methods in Fluids* 83 (2) (2017) 205–219.
- [16] R. Yondo, E. Andrés, E. Valero, A review on design of experiments and surrogate models in aircraft real-time and many-query aerodynamic analyses, *Progress in Aerospace Sciences* 96 (2018) 23–61.
- [17] J. Yu, C. Yan, Z. Jiang, W. Yuan, S. Chen, Adaptive non-intrusive reduced order modeling for compressible flows, *Journal of Computational Physics* 397 (2019) 108855. doi:<https://doi.org/10.1016/j.jcp.2019.07.053>.
- [18] F. Alsayyari, Z. Perkó, M. Tiberga, J. L. Kloosterman, D. Lathouwers, A fully adaptive nonintrusive reduced-order modelling approach for parametrized time-dependent problems, *Computer Methods in Applied Mechanics and Engineering* 373 (2021) 113483. doi:<https://doi.org/10.1016/j.cma.2020.113483>.
- [19] K. Kunisch, S. Volkwein, Optimal snapshot location for computing POD basis functions, *ESAIM: Mathematical Modelling and Numerical Analysis* 44 (3) (2010) 509–529.
- [20] Q. Wang, N. Ripamonti, J. S. Hesthaven, Recurrent neural network closure of parametric POD-Galerkin reduced-order models based on the Mori-Zwanzig formalism, *Journal of Computational Physics* 410 (2020) 109402. doi:<https://doi.org/10.1016/j.jcp.2020.109402>.
- [21] P. Phalippou, S. Bouabdallah, P. Breitenkopf, P. Villon, M. Zarroug, 'On-the-fly' snapshots selection for proper orthogonal decomposition with application to nonlinear dynamics, *Computer Methods in Applied Mechanics and Engineering* 367 (2020) 113120. doi:<https://doi.org/10.1016/j.cma.2020.113120>.
- [22] Z. Luo, Q. Ou, Z. Xie, Reduced finite difference scheme and error estimates based on POD method for non-stationary Stokes equation, *Applied Mathematics and Mechanics* 32 (2011) 847–858.

- [23] X. Zhang, P. Zhang, A reduced high-order compact finite difference scheme based on proper orthogonal decomposition technique for KdV equation, *Applied Mathematics and Computation* 339 (2018) 535–545.
- [24] B. Xu, X. Zhang, An efficient high-order compact finite difference scheme based on proper orthogonal decomposition for the multi-dimensional parabolic equation, *Advances in Difference Equations* 2019 (1) (2019) 341.
- [25] O. Lass, S. Volkwein, POD-Galerkin schemes for nonlinear elliptic-parabolic systems, *SIAM Journal on Scientific Computing* 35 (3) (2013) A1271–A1298.
- [26] S. Ullmann, M. Rotkvic, J. Lang, POD-Galerkin reduced-order modeling with adaptive finite element snapshots, *Journal of Computational Physics* 325 (2016) 244–258.
- [27] E. N. Karatzas, F. Ballarin, G. Rozza, Projection-based reduced order models for a cut finite element method in parametrized domains, *Computers & Mathematics with Applications* 79 (3) (2020) 833–851.
- [28] Z. Luo, H. Li, Y. Zhou, X. Huang, A reduced FVE formulation based on POD method and error analysis for two-dimensional viscoelastic problem, *Journal of Mathematical Analysis and Applications* 385 (1) (2012) 310–321.
- [29] S. Lorenzi, A. Cammi, L. Luzzi, G. Rozza, POD-Galerkin method for finite volume approximation of Navier–Stokes and RANS equations, *Computer Methods in Applied Mechanics and Engineering* 311 (2016) 151–179.
- [30] G. Stabile, G. Rozza, Finite POD-Galerkin stabilised reduced order methods for the parametrised incompressible Navier-Stokes equations, *Computers & Fluids* 173 (2018) 273–284.
- [31] K. Li, T.-Z. Huang, L. Li, S. Lanteri, L. Xu, B. Li, A reduced-order discontinuous Galerkin method based on POD for electromagnetic simulation, *IEEE Transactions on Antennas and Propagation* 66 (1) (2018) 242–254.
- [32] K. Li, T.-Z. Huang, L. Li, S. Lanteri, POD-based model order reduction with an adaptive snapshot selection for a discontinuous Galerkin approximation of the time-domain Maxwell’s equations, *Journal of Computational Physics* 396 (2019) 106–128.
- [33] Z. Luo, Proper orthogonal decomposition-based reduced-order stabilized mixed finite volume element extrapolating model for the nonstationary incompressible Boussinesq equations, *Journal of Mathematical Analysis and Applications* 425 (1) (2015) 259–280.
- [34] Z. Luo, J. Gao, A POD reduced-order finite difference time-domain extrapolating scheme for the 2D Maxwell equations in a lossy medium, *Journal of Mathematical Analysis and Applications* 444 (1) (2016) 433–451.
- [35] Z. Luo, F. Teng, A reduced-order extrapolated finite difference iterative scheme based on POD method for 2D sobolev equation, *Applied Mathematics and Computation* 329 (15) (2018) 374–383.
- [36] Z. Luo, F. Teng, H. Xia, A reduced-order extrapolated Crank-Nicolson finite spectral element method based on POD for the 2D non-stationary boussinesq equations, *Journal of Mathematical Analysis and Applications* 471 (1-2) (2019) 564–583.

- [37] Z. Luo, J. Shiju, A reduced-order extrapolated Crank-Nicolson collocation spectral method based on proper orthogonal decomposition for the two-dimensional viscoelastic wave equations, *Numerical Methods for Partial Differential Equations* 36 (1) (2020) 49–65.
- [38] Z. Luo, H. Ren, A reduced-order extrapolated finite difference iterative method for the riemann-liouville tempered fractional derivative equation, *Applied Numerical Mathematics* 157 (2020) 307–314.
- [39] Z. Luo, W. Jiang, A reduced-order extrapolated technique about the unknown coefficient vectors of solutions in the finite element method for hyperbolic type equation, *Applied Numerical Mathematics* 158 (2020) 123–133.
- [40] Y. Zhou, Y. Zhang, Y. Liang, Z. Luo, A reduced-order extrapolated model based on splitting implicit finite difference scheme and proper orthogonal decomposition for the fourth-order nonlinear rosenau equation, *Applied Numerical Mathematics* 162 (2021) 192–200.
- [41] M. Barrault, Y. Maday, N. C. Nguyen, A. T. Patera, An 'empirical interpolation' method: application to efficient reduced-basis discretization of partial differential equations, *Comptes Rendus Mathematique* 339 (9) (2004) 667–672.
- [42] S. Chaturantabut, D. C. Sorensen, Nonlinear model reduction via discrete empirical interpolation, *SIAM Journal on Scientific Computing* 32 (5) (2010) 2737–2764.
- [43] C. Fabien, E. Alexandre, L. Tony, A nonintrusive reduced basis method applied to aeroacoustic simulations, *Advances in Computational Mathematics* 41 (2015) 961–986.
- [44] C. Audouze, F. D. Vuyst, P. B. Nair, Nonintrusive reduced-order modeling of parametrized time-dependent partial differential equations, *Numerical Methods for Partial Differential Equations* 29 (5) (2013) 1587–1628.
- [45] R. Chakir, Y. Maday, P. Parnaudeau, A non-intrusive reduced basis approach for parametrized heat transfer problems, *Journal of Computational Physics* 376 (2019) 617–633.
- [46] N. Dal Santo, S. Deparis, L. Pegolotti, Data driven approximation of parametrized pdes by reduced basis and neural networks, *Journal of Computational Physics* 416 (2020) 109550. doi:<https://doi.org/10.1016/j.jcp.2020.109550>.
- [47] M. Kast, M. Guo, J. S. Hesthaven, A non-intrusive multifidelity method for the reduced order modeling of nonlinear problems, *Computer Methods in Applied Mechanics and Engineering* 364 (112947) (2020). doi:<https://doi.org/10.1016/j.cma.2020.112947>.
- [48] X. Sun, X. Pan, J.-I. Choi, Non-intrusive framework of reduced-order modeling based on proper orthogonal decomposition and polynomial chaos expansion, *Journal of Computational and Applied Mathematics* 390 (2021) 113372. doi:<https://doi.org/10.1016/j.cam.2020.113372>.
- [49] F. Stefania, D. Luca, M. Andrea, A comprehensive deep learning-based approach to reduced order modeling of nonlinear time-dependent parametrized pdes, *Journal of Scientific Computing* 87 (61) (2021). doi:<https://doi.org/10.1007/s10915-021-01462-7>.
- [50] W. Chen, Q. Wang, J. S. Hesthaven, C. Zhang, Physics-informed machine learning for reduced-order modeling of nonlinear problems, *Journal of Computational Physics* 446 (110666) (2021). doi:<https://doi.org/10.1016/j.jcp.2021.110666>.

- [51] K. L. Judd, L. Maliar, S. Maliar, R. Valero, Smolyak method for solving dynamic economic models: Lagrange interpolation, anisotropic grid and adaptive domain, *Journal of Economic Dynamics and Control* 44 (2014) 92–123.
- [52] T. Gerstner, M. Griebel, Numerical integration using sparse grids, *Numerical Algorithms* 18 (1998). doi:<https://doi.org/10.1023/A:1019129717644>.
- [53] D. Loukrezis, U. Römer, H. D. Gerssem, Assessing the performance of Leja and Clenshaw-Curtis collocation for computational electromagnetics with random input data, *International Journal for Uncertainty Quantification* 9 (1) (2019) 33–57.
- [54] C. K. I. Williams, C. E. Rasmussen, Gaussian processes for regression, in: *Proceedings of the 8th international conference on neural information processing systems*, MIT press, 1995, pp. 514–520.
- [55] C. E. Rasmussen, C. K. I. Williams, *Gaussian processes for machine learning*, MIT press, 2006.